The spatiotemporal structure of precipitation in Indian monsoon depressions

Article

Published Version

It is advisable to refer to the publisher's version if you intend to cite from the work. See Guidance on citing.

www.reading.ac.uk/centaur

RMetS

Royal Meteorological Society

The spatiotemporal structure of precipitation in Indian monsoon depressions

Kieran M. R. Hunt,[a]* Andrew G. Turner[a,b] and David E. Parker[c]

[a]*Department of Meteorology, University of Reading, UK*
[b]*NCAS–Climate, University of Reading, UK*
[c]*Met Office Hadley Centre, Exeter, UK*

*Correspondence to: K. M. R. Hunt, Department of Meteorology, University of Reading, Reading, RG6 6BB, UK.
E-mail: k.hunt@pgr.reading.ac.uk

Indian monsoon depressions are synoptic-scale events typically spun up in the Bay of Bengal. They usually last 4–6 days, during which they propagate northwestward across the Indian subcontinent before dissipating over northwest India or Pakistan. They can have a significant effect on monsoon precipitation, particularly in primarily agrarian northern India, and therefore quantifying their structure and variability and evaluating these in numerical weather prediction (NWP) models and general circulation models (GCMs) is of critical importance. In this study, satellite data from *CloudSat* and recently concluded *Tropical Rainfall Measuring Mission* (*TRMM*) missions are used in conjunction with an independently evaluated tracking algorithm to form a three-dimensional composite image of cloud structure and precipitation within monsoon depressions. The composite comprises 34 depressions from the 1998–2014 *TRMM* mission and 12 from the 2007–present *CloudSat* mission and is statistically robust enough to allow significant probing of the spatiotemporal characteristics of moisture and hydrometeor fields. Among the key results of this work are the following: the discovery and characterization of a bimodal, diurnal cycle in surface precipitation; the first picture of the structure of cloud type and density in depressions, showing that deep convection dominates south of the centre and prominent cirrus throughout; the first composite picture of vertical hydrometeor structure in depressions, showing significant precipitation for hundreds of kilometres outside the centre and well past the mid-troposphere; and a novel discussion of drop-size distributions (showing significant uniformity across the depression) and the resulting latent heat profiles, showing that average heating rates near the centre can reach $2 \, \mathrm{K \, h^{-1}}$.

Key Words: monsoon; depression; *TRMM*; *CloudSat*; precipitation; satellite

Received 8 January 2016; Revised 8 August 2016; Accepted 15 August 2016; Published online in Wiley Online Library

1. Introduction

Indian monsoon depressions (MDs) are synoptic-scale disturbances that originate near the head of the Bay of Bengal or in the Indian monsoon trough region (Sikka, 1977; Krishnamurthy and Shukla, 2007; Hurley and Boos, 2015; Hunt *et al.*, 2016). With a typical frequency of 2–5 per summer and an average duration of 4–6 days (Godbole, 1977; Saha *et al.*, 1981; Sarker and Choudhary, 1988; Hurley and Boos, 2015; Hunt *et al.*, 2016), they are an important feature of the Indian monsoon, capable of providing very heavy precipitation across much of northern India (Godbole, 1977; Stano *et al.*, 2002; Hunt *et al.*, 2016), which, as a predominantly agrarian society, relies prominently on rainfall. It is therefore crucial to have a clear understanding of the hydrometeor structure and moist thermodynamic processes of these events. Short and Nakamura (2000) and Fu and Liu (2001) provided the first analyses of the vertical structure of rainfall rates in the tropics using satellite data, preceding the case study of the three 1999 depressions by Stano *et al.* (2002). Since then, there have been numerous further studies using the *Tropical Rainfall Measuring Mission* (*TRMM*), but none exploiting the depth of such satellite data on the nearly 40 MDs that have occurred since the launch of *TRMM*. Recently, Bowman and Fowler (2015) used *TRMM* to examine the diurnal structure of tropical cyclones, showing that precipitation within 500 km of the centre had a diurnal cycle with a maximum in the early morning.

We remain, therefore, without even a basic understanding of the moist processes that occur in MDs. Whilst it has been known for some time that the maximum surface precipitation is to be found several hundred kilometres southwest of the depression

Table 1. An overview of the *TRMM* algorithms and datasets used in this study.

Code	Name	Dependencies	Outputs Used	Citation
2A23	PR qualitative	PR	Rain type Bright band Storm height	Awaka *et al.* (1997)
2A25	PR profile	PR 2A23	Rain rate Estimated surface rain rate	Iguchi *et al.* (2000)
2B31	PR combined	PR TMI 2A23	Snow density Graupel density Drop size distribution Latent heating	Haddad *et al.* (1997a,b)
3B42	*TRMM* & Other sensors – 3 hourly	PR TMI 2A23 Other satellites	Gridded global precipitation	Huffman *et al.* (1995, 1997, 2007, 2010); Huffman (1997)

centre (Roy and Roy, 1930; Ramanathan and Ramakrishnan, 1933; Mull and Rao, 1949; Desai, 1951; Petterssen, 1956; Mooley, 1973; Godbole, 1977; Daggupaty and Sikka, 1977; Stano *et al.*, 2002; Yoon and Chen, 2005; Hunt *et al.*, 2016), there is no certainty on the generating mechanism and several prevailing theories result: the westward axial tilt of the core with height, collocation with a lower-troposphere convergence maximum, cyclonic mixing of cool monsoon circulation with warm, moist southwesterlies from the Bay of Bengal, or even some combination of these. Most recently, Yoon and Chen (2005) suggested that this asymmetry was a consequence of MD water-vapour flux convergence coupling with longer-period modes of monsoon variability, but showed only that these (10−20 and 30−60 days) modes could enhance or suppress the MD rainfall, not that they were necessarily the reason for the location of its maximum.

Sørland and Sorteberg (2015) tracked 39 monsoon low-pressure systems (LPSs) associated with daily extreme rainfall events as given by the gridded gauge precipitation dataset of the India Meteorological Department (Rajeevan *et al.*, 2005, 2006); they attempted to correlate precipitation rates in these LPSs with prognostic parameters, finding the most significant correlation was with 750 hPa vertical velocity. They also posited that a strong negative correlation between surface rain rate and 950 hPa temperature indicated that evaporative cooling from precipitation was responsible for the lower tropospheric cold core (e.g. Godbole, 1977; Hurley and Boos, 2015; Hunt *et al.*, 2016) of MDs.

This study comprises three main parts: after discussing the data and methodology in section 2, we will look at *TRMM* and *CloudSat*-derived composites in section 3, compare these with a specific case study in section 4 and then explore the diurnal pattern in section 5, before concluding in section 6.

2. Methodology

2.1. Data

2.1.1. Tropical Rainfall Measuring Mission

This study makes substantial use of data from the *TRMM* satellite mission, which was operational between December 1997 and October 2014 (Simpson *et al.*, 1988, 1996; Kummerow *et al.*, 1998, 2000). It accommodated five instruments: the *TRMM* Microwave Imager (TMI); the Precipitation Radar (PR); the Visible Infrared Radiometer (VIRS); the Cloud and Earth Radiant Energy Sensor (CERES); and the Lightning Imaging Sensor (LIS). Throughout, we will be concerned with data output products that inherits from the first three. The PR was a *Ku*-band radar working at 13.8 GHz (Kawanishi *et al.*, 1993, 2000) that provided high spatiotemporal resolution three-dimensional precipitation measurements over both land and ocean and is the primary source of these datasets; for a summary of which *TRMM* data are used in this study, see Table 1. The level-2 algorithms (those prefixed with '2') retain

Table 2. An overview of the *CloudSat* datasets used in this study.

Code	Outputs used	Citation
2B-GEOPROF	Cloud mask, cloud flag, radar reflectivity	Marchand *et al.* (2008)
2B-CLDCLASS	Cloud scenario	Sassen and Wang (2008)
2B-FLXHR	Longwave and short-wave radiative heating effects	L'Ecuyer *et al.* (2008)
2C-RAIN-PROFILE	Liquid and ice precipitation densities	L'Ecuyer and Stephens (2002)
2C-PRECIP-COLUMN	Surface precipitation flag and rate	Haynes *et al.* (2009)

the resolution and footprint of the original satellite swath, a 220 km wide track at 4 km × 4 km × 250 m (80 vertical levels)*; in contrast, the level-3 algorithm used here has global coverage between the 50th parallels and is a multi-satellite product, also comprising inputs from *GMS*, *GOES-E*, *GOES-W*, *Meteosat-7*, *Meteosat-5* and *NOAA-12*. This surface precipitation product has a resolution of 0.25° × 0.25°.

2.1.2. CloudSat

CloudSat is a National Aeronautics and Space Administration (NASA) polar-orbiting *A-Train* satellite primarily equipped with a 94 GHz cloud-profiling active reflectivity radar (Stephens *et al.*, 2002, 2008), which measures the backscattered energy from clouds and precipitation. It has been in almost continuous operation since June 2006 and, via the CloudSat Data Processing Centre at Colorado State University, the mission releases numerous cloud quantification and thermodynamic datasets. A summary of those datasets used in this study is given in Table 2. The radar measures nadir only and therefore the output swaths have zero width; the along-track resolution is 1.7 km and there are 125 vertical levels at a resolution of 250 m.

2.1.3. ERA-Interim

We will make occasional use of the European Centre for Medium-Range Weather Forecasts (ECMWF) authored ERA-Interim (ERA-I) reanalysis product. This has six-hourly global coverage at T255 (∼ 77 km at the equator) resolution (Dee *et al.*, 2011). Quite a number of products are available on a global Gaussian grid, either at the surface, on pressure levels (37 in total, from 1000 to 1 hPa) or at sigma or potential vorticity levels. There are also some precipitation-related datasets within ERA-I, but, as a prognostic variable, it has poor skill when compared with satellite observations (Liu *et al.*, 2014).

---

*The *TRMM* orbit was boosted in August 2001, increasing the swath width to 250 km with a footprint of 5 km × 5 km.

2.2. Compositing

Hunt *et al.* (2016) outlined a wind-thresholded vorticity-pressure feature-tracking algorithm applied to ERA-Interim reanalysis data over the Indian subcontinent for the period 1979–2014, wherein they identified and corroborated 106 MDs with genesis over either the Bay of Bengal or the subcontinent itself; we shall be using the relevant subset of that data for the *TRMM (CloudSat)* operation period: 34 (12) depressions during 1998–2014 (2007–present). Furthermore, in some instances (usage of the 3B42 data) we replicate the rotation-composition method of Hunt *et al.* (2016) (also used in e.g. Catto *et al.* 2010): for each MD time step, the depression heading is calculated; the data are then reoriented, centralized and composited on to a new grid such that the composite heading is due north and the 850 hPa relative vorticity maximum lies above the latitude–longitude origin.

Where data are sparser, compositing the data in this manner is not statistically robust. Instead we can boost the sample size artificially by collapsing the azimuthal dimension and treating the composite data as a function only of radius and height. This introduces a degeneracy that we can exploit to examine an asymmetry of our choice. The largest mode of spatial asymmetry in MDs is caused by the presence of the Himalayas (Hunt and Parker, 2016; Hunt *et al.*, 2016) and so we shall henceforth define the pseudoradial coordinate, with magnitude equal to the radius and the sign of the normalized latitude; for example, a point 440 km westsouthwest (or any bearing between 90° and 270°) of the centre would have a pseudoradius of −440 km (or −4° using the 111 km per degree employed in this study). This method was developed with *CloudSat* data in mind, but for consistency has been extended to discussions of vertical structure derived from *TRMM* products.

3. Composite structure

Firstly, we shall build a three-dimensional composite in the manner outlined in section 2.2. It is important to gauge the mean structure of precipitation and cloud attributes for two reasons: so that we have a fundamental base for further analysis and because, as the leading-order moment, this is what any model should primarily be tested against.

3.1. Hydrometeor distributions

Arguably the outright most important feature of an MD is surface precipitation, so we shall open our discussion of mean structure with this field. Figure 1 presents this in two ways: (i) rotated, i.e. the data from each time step are rotated such that the depression propagates along zero bearing, and (ii) unrotated.

Note that Figure 1(a) comprises the same data as Figure 4(a) from Hunt *et al.* (2016). The most striking difference between the two, noting the different colour scales, is the magnitude of the central maximum; there are two factors causing it to be reduced in the rotated composite: implicit smoothing during interpolation on to the rotated grid and the temporal variability of the location of the maximum precipitation in the rotated coordinates (providing extra variance associated with the spread of headings). We should note that both of these factors are unique to precipitation fields, which have categorically the highest variance of any common meteorological variable and which uniquely do not have composite extrema collocated with the depression centre. As discussed previously, we see the maximum surface precipitation located several hundred kilometres southwest; it has a maximum magnitude of over 70 mm day^{-1} at 1.4°S, 1.7°W and falls away quickly except for a band in the east representing orographic rainfall along the coast of the Bay of Bengal.

We are now in a position to explore the composite vertical structure of precipitation. The simplest manifestation of this is rain rate, shown in Figure 2; ground clutter returns and any missing data are not included in the composite, therefore any part of the composite with no useful data is shown as the background grey colour. The seemingly very high rainfall rates shown near the surface are an artefact of this process: there, only very high radar reflectivities can surpass ground clutter. The general structure is what we might expect on consideration of the surface precipitation shown in Figure 1; indeed, the data from (b) of that figure are collapsed on to the pseudoradius coordinate for illustration. Here, the asymmetry is stark: the strongest rains both at the surface and aloft are found several hundred kilometres away from the centre, in the southern half. We note also that the rainfall rates in the upper mid-troposphere (~ 7 km) are proportional to those much nearer the surface, implying that most surface rainfall is the result of deep convective processes. The effect of the Himalayas in the northern half can also be seen: the ratio of rainfall aloft to that near the surface is higher in the south (e.g. 10–15°) than the north, implying orographic forcing there.

Now we have an idea of the rainfall rates throughout the composite MD, we can use data from *TRMM* 2B31 to estimate raindrop size distributions (DSDs); doing so will further assist our investigation into the physics driving hydrometeors in MDs. We obviously cannot show the varying DSDs throughout the composite, so instead a figure showing the modal raindrop size throughout the MD with some selected DSDs is given (Figure 3). Calculating these distributions is non-trivial and it is beyond the scope of this study to describe the full calculation here; for a full derivation, the reader is encouraged to visit Haddad *et al.* (1997a). What the figure shows us is that there is a well-defined area where the *TRMM* 2B31 algorithm believes that there is rain and within it the modal drop size has fairly low variance. It is
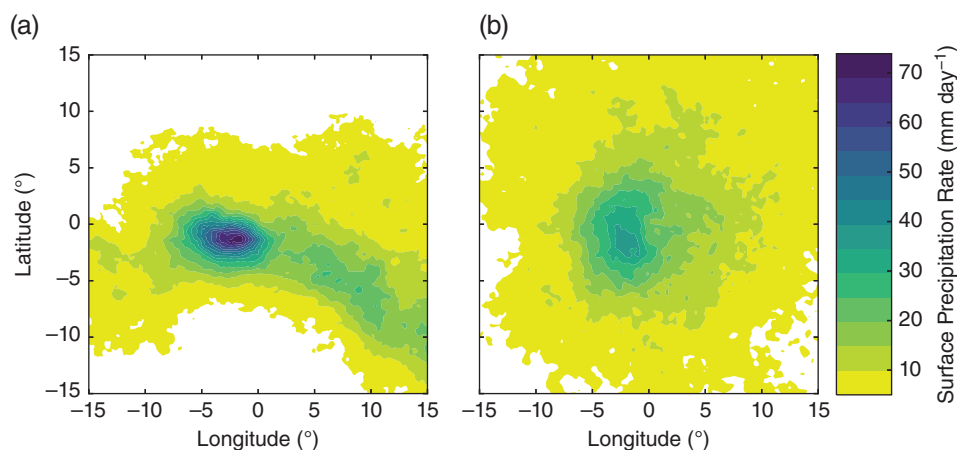

Figure 1. Composite mean surface precipitation (mm day^{-1}) from *TRMM* 3B42 for depressions 1997–2014. (a) No rotation during compositing. (b) The rotated composite, where each time step is rotated such that the depression is heading due north (i.e. up the page).
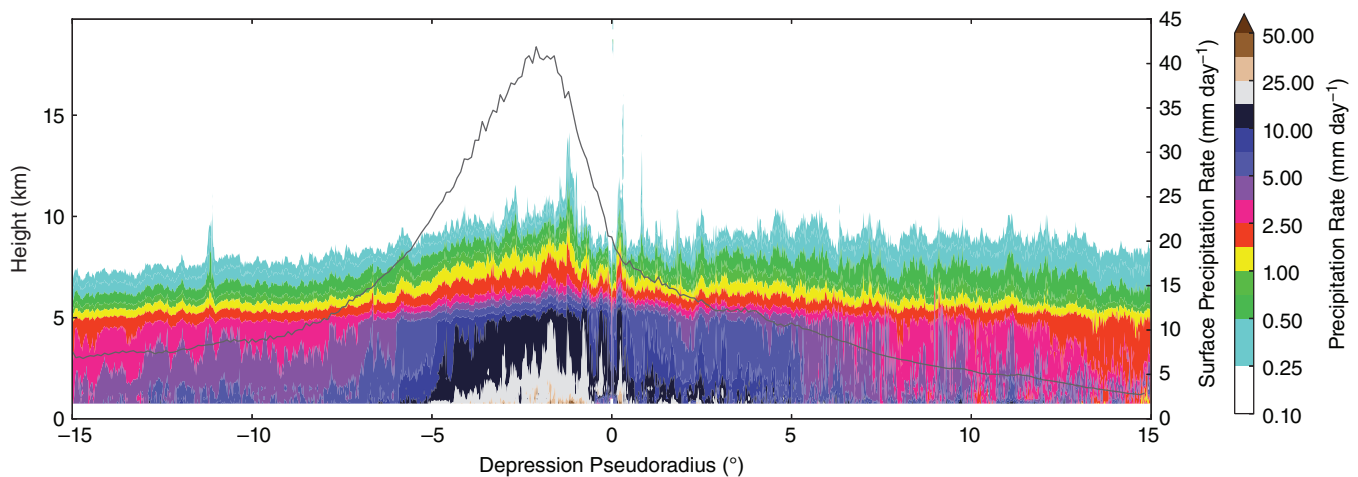
Figure 2. Composite vertical profile of rain rate (mm day^{-1}, coloured contours) from *TRMM* 2A25 as a function of pseudoradius. Overlaid as a dark grey line for illustration is the (unrotated) composite surface rain rate (mm day^{-1}, right axis) from *TRMM* 3B42 (see Figure 1(a)), also as a function of pseudoradius. Note that the lowest contour is coloured white and the background grey.
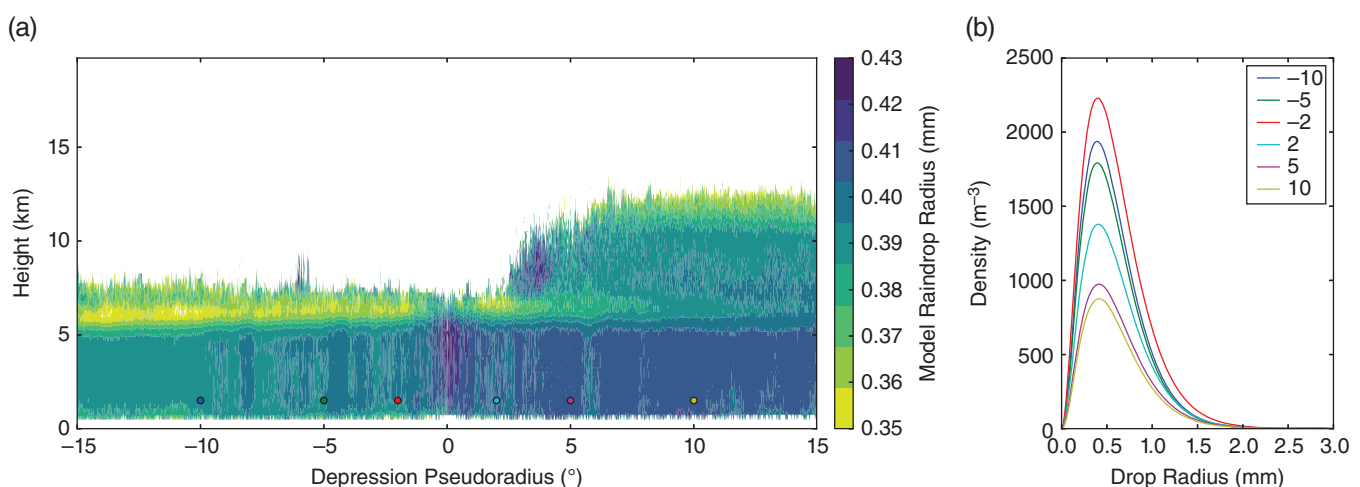

Figure 3. Modal raindrop size (mm, radius) throughout the composite, calculated from the drop size distribution parameters in *TRMM* 2B31. (b) Full distributions for selected pseudoradii at a height of 1.5 km, the locations of which are indicated by dots in (a).

particularly interesting to note that, whilst the highest rainfall rates (see Figure 2) and highest raindrop number densities are found to the south of the centre, the largest drops tend to be found at the centre itself. Raindrop size appears, at least south of the centre, to be fairly uniform with height until within a kilometre or so of the apparent cloud top. This uniformity indicates that these southern areas are well mixed in depth, in contrast with the centre itself, where the drop size generally increases with height, implying strong ascent there.

Finally, we can complete our discussion on the composite hydrometeor structure by considering the distribution of frozen water in MDs. Figure 4 shows the expected densities of snow and graupel in the composite MD, as well as the average freezing, bright band and storm heights. The maxima for snow and graupel densities are to be found directly above the highest rain rates, indicating that an area of deep convection is responsible for both. This is supported by the graupel having a comparable (or even greater) density to snow, indicating the presence of some mixing process allowing the aggregation and refreezing of the latter into the former. One might be surprised to see that there is a very low frozen hydrometeor density in the north around the Himalayas, but this is simply explained: the climatological freezing height in the Himalayan foothills is over 5 km, but almost all rainfall there is orographic and happens below this altitude, resulting in very little ice formation. The height of the bright band gives us an indication of where extant falling snow is melting most rapidly – we do not expect this to be necessarily at the freezing height, because there is a fairly shallow temperature gradient and

ice has a finite heat capacity. The difference between the bright band and freezing heights can be interpreted as a weak metric for vertical wind speed.

3.2. Cloud scenario

The importance of classifying clouds in a hydrometeor-based compositing study such as this is clear: the presence of different types of cloud represent the dominance of crucially different precipitating and non-precipitating mechanisms in the atmosphere. If we can constrain the types most likely to be present throughout the MD, we can evaluate the physics behind their representation in GCMs and NWPs better.

The *CloudSat* 2B-CLDCLASS product classifies cloud types by using constraints such as spatial cloud properties, cloud temperature, the existence of precipitation and radiance measurements from other *A-Train* satellites (Wang and Sassen, 2007). The category bins are as follows: clear, cirrus, altostratus, altocumulus, stratus, stratocumulus, cumulus, nimbostratus and deep convection, all of which can be found in the Tropics (Sassen and Wang, 2008) and indeed over India. Regridding discrete, qualitative data must be done carefully: we cannot simply compute an interpolating function or calculate distribution moments; instead we must consider the mode. Heeding this, the modal cloud-type composite is given in Figure 5. Here, the hue is a function of the most common type (excluding clear sky); the transparency is zero (i.e. fully opaque) if the ratio of the modal frequency (including clear sky) is greater than or equal to 0.5;
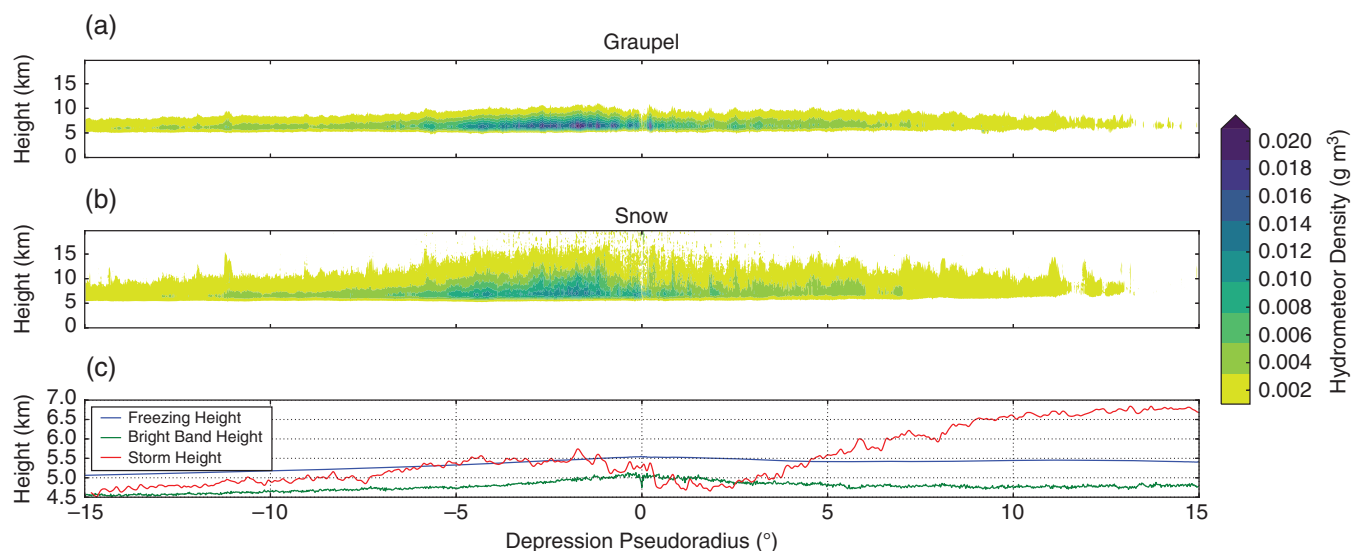
Figure 4. Composite vertical profile of (a) graupel $(g\,m^{-3})$ and (b) snow $(g\,m^{-3})$ densities as a function of pseudoradius, from *TRMM* 2B31. (c) Structures of the bright band, storm and freezing heights, from *TRMM* 2A23. Note that height scales differ between (a, b) and (c). The colour scale is the same for both relevant panels.
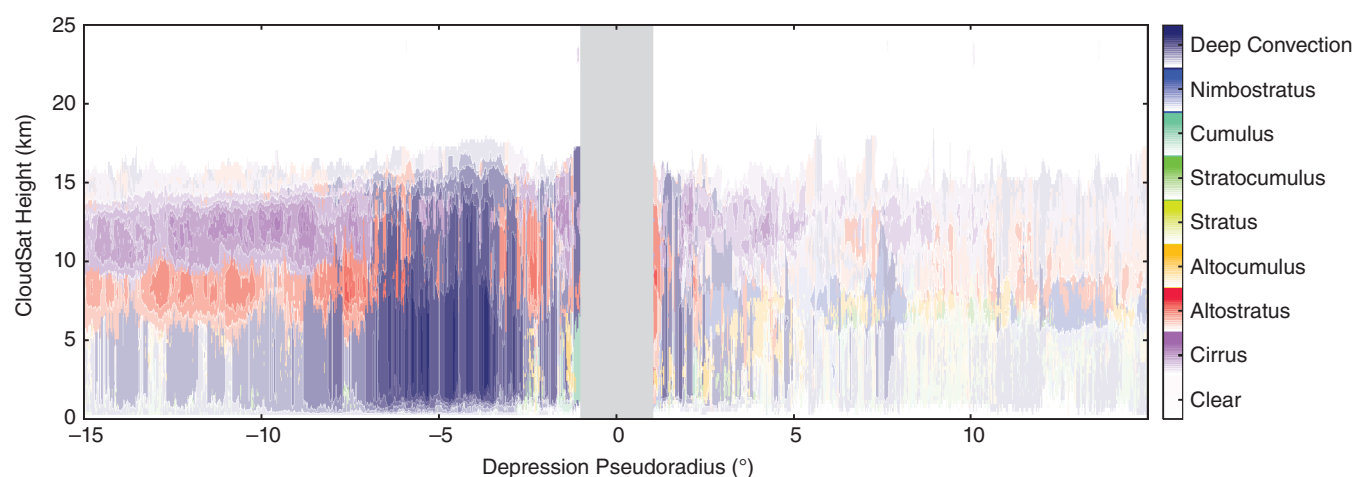

Figure 5. Modal cloud scenario in the composite, determined by *CloudSat* 2B-CLDCLASS. Differing hues represent varying cloud types, with the transparency in each case proportional to the ratio of the modal value and the number of overpasses up to a value of 0.5. Parts of the composite not comprising at least ten satellite overpasses are not shown here. We remind the reader that *CloudSat* height is referenced above the geoid, rather than necessarily the Earth's surface.

below this value they are directly proportional. For example, if the modal cloud type in a particular instance was altostratus and it was present in 30% of the composite, it would be represented in the figure as a red hue with 60% opacity (40% transparency).

The figure shows that despite all clouds types being present, there are three distinct domains of cloud structure. In the far south, there is the stratification one might expect in a typical tropical environment (Stein *et al.*, 2011): convective clouds in the lower troposphere, becoming altostratus in the mid-troposphere and cirrus tending towards the tropopause; as we move closer to the centre, the initially low-level convective clouds suddenly dominate throughout the height of the troposphere, even rising higher than the cirrus further afield. In the north, however, whilst there is some deep convection much closer to the centre, it tends to be much more mixed: there is some mid-level stratus present, indicating that the Himalayas are forcing orographic cloud there. We might suppose that if the height coordinate were measured from the actual surface, rather than the geoid, in the north we would recover dominant stratus at/near the surface; this is indeed the case, although it is not shown here.

We can use these data to explore a little further: by considering the fraction of overpasses that detect cloud (as opposed to clear sky) to generate a cloud-cover variable; the result is shown in Figure 6. Here, both the composite from *CloudSat* overpasses and an equivalently constructed composite from *ERA-I* are shown. Both have clearly captured some structure, but there are stark

differences: the ERA-I composite has substantially less cloud in the mid-troposphere, where it suggests almost no cover at all, and in the lower troposphere, where the deep convection is poorly resolved. The ERA-I derived composite does, however, capture the asymmetry and the high-level cloud structure well compared with *CloudSat*. Unfortunately, since the comparison of the global all-year climatologies of satellite and reanalysis cloud cover by Jakob (1999), there has been no further research on comparison of these cloud products in the tropics.

Now, we wish to explore the convective and non-convective spatial regimes of the composite MD. Such analysis has been done before using *contoured frequency by altitude diagrams* (CFADs), for single events (e.g. Yuter and Houze, 1995), domain composites (e.g. Liu *et al.*, 2010) and system composites (e.g. Hence and Houze, 2011). CFADs display normalized histograms of radar reflectivities as a function of height and have specifically been used for cloud-type analysis with both the 13.8 GHz *TRMM* PR (Houze *et al.*, 2007) and the 94 GHz *CloudSat* radar (Young, 2015). We hypothesize three distinct regimes from Figure 5: generally tropical (e.g. $-10°$), strongly convective (e.g. $-4°$) and generally orographic (e.g. $10°$). CFADs for these pseudoradii (with an inclusive envelope of $0.4°$ on each side) are shown in Figures 7 and 8 for *TRMM* and *CloudSat* radar reflectivities, respectively.

Houze *et al.* (2007) generated 13.8 GHz reflectivity CFADs for composite stratiform and convective systems within the Indian
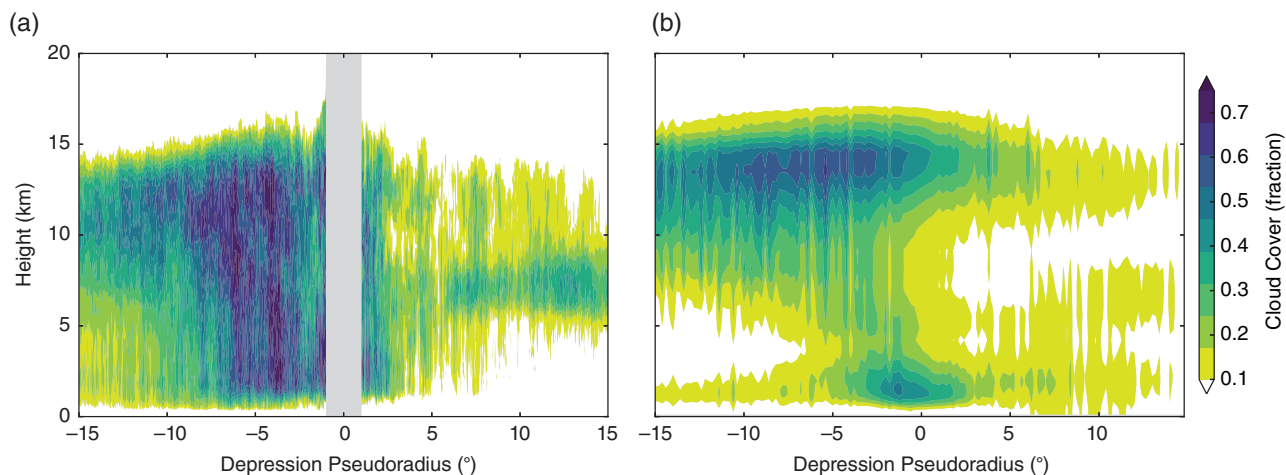
Figure 6. (a) Cloud cover (fraction of unity) as a function of pseudoradius, as calculated from composite 2B-CLDCLASS data. (b) As (a), using ERA-I data. For consistency, both are composited using the same technique.
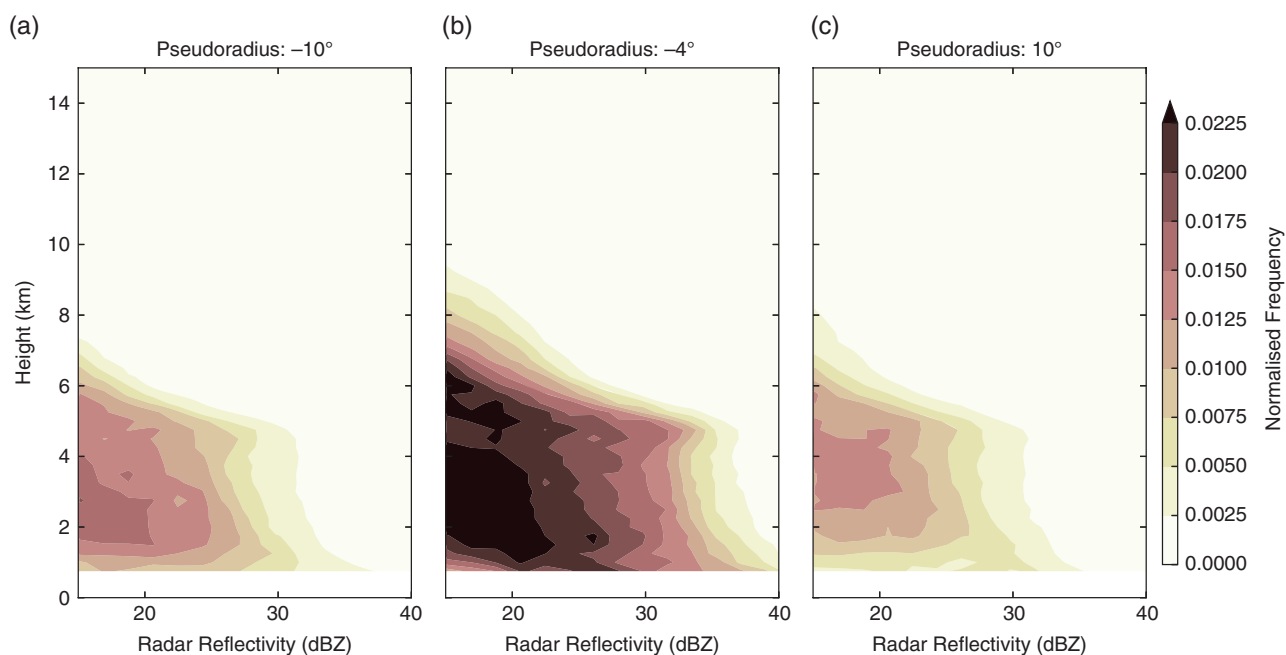

Figure 7. Contoured frequency by altitude diagram (CFAD: Yuter and Houze, 1995) for effective radar reflectivity at 13.8 GHz (dBZ) from *TRMM* 2A25, at pseudoradii of (a) −10°, (b) −4° and (c) 10°. The abscissa starts at 15 dBZ, the approximate value of the *TRMM* PR sensitivity threshold.

monsoon. Comparing Figure 7 with Figure 27 of Houze *et al.* (2007), we see that the CFAD at a pseudoradius of −4° has a very strong resemblance to their composite of convective cloud structure. Conversely, the CFAD at 10° pseudoradius has a clearly stratiform structure, as we might expect from our earlier analysis. Finally, at a pseudoradius of −10°, we note more of a mixed regime, with a slight preference for convective structure, albeit with a less common occurence than that observed nearer the centre. Repeating this analysis for Figure 8 by comparison with the 94 GHz reflectivity CFAD composites over Africa from Young (2015), we build a very simlar picture: mixed with occasional convection at −10°; common convection at −4°; and common stratiform at 10°. Here we also note the strong attentuation in the higher frequency *CloudSat* radar reflectivity, particularly below 4 km, as also noted by Sindhu and Bhat (2013).

We can attempt to delineate these regimes further by considering the 'rain type' product from *TRMM* 2A23 alongside the simultaneous estimated surface rainfall rate to explore any spatial coherence in precipitation attributable to convective and stratiform processes, respectively. The *TRMM* 2A23 rain-type algorithm uses a combination of two methods (Awaka *et al.*, 2007) to determine what type of process rain, if existent, is likely to be have been generated by. The first, the *V-method*,

determines that precipitation is stratiform if a bright band exists and convective if there is no bright band but the radar reflectivity is above a threshold of 39 dBZ; otherwise, it determines it to be 'other'. The second, the *H-method* (based on Steiner *et al.*, 1995), requires several criteria (39 dBZ reflectivity threshold, high signal-to-noise ratio) to make the determination of convective precipitation; if these criteria are not met but rain is still certain, it is determined to be stratiform; if the signal-to-noise ratio is too weak but rain is possible, it is assigned 'other'. Subsequently, the 2A23 rain-type algorithm determines that precipitation is definitely stratiform if it is V-stratiform or H-stratiform/other and correspondingly convective if it is V-convective/other or H-convective. If the H-method and V-method explicitly disagree, preference is given to the V-method; this, with other sensible combinations comprise the maybe and probable levels of each type. If neither method can make a determination, but rain is certain, it is given the 'other' category.

Figure 9 shows the composite proportion of *TRMM* 2A25 estimated surface precipitation rate definitely attributable to convective and stratiform systems according to the *TRMM* 2A23 rain-type algorithm, as well as the remainder. Overall, approximately half of the rainfall is attributed, but the algorithm struggled considerably around the Himalayas and south of the
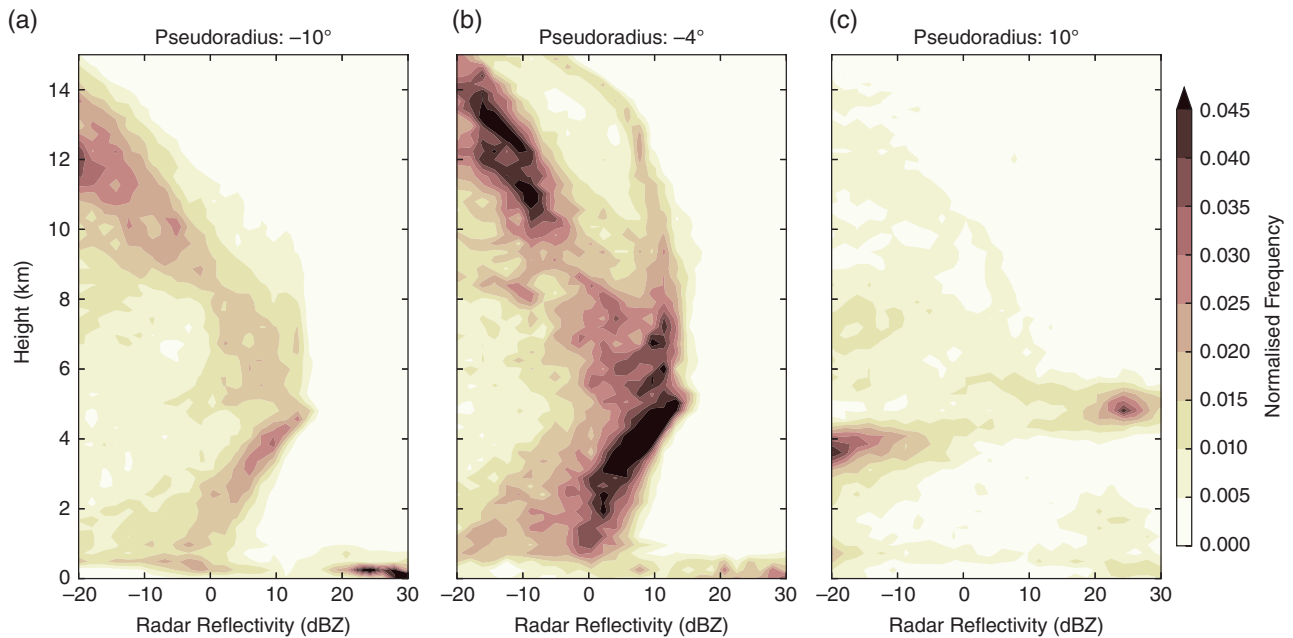
Figure 8. As Figure 7 but for radar reflectivities at 94 GHz from *CloudSat* 2B-GEOPROF. Again, at pseudoradii of (a) −10°, (b) −4° and (c) 10°.
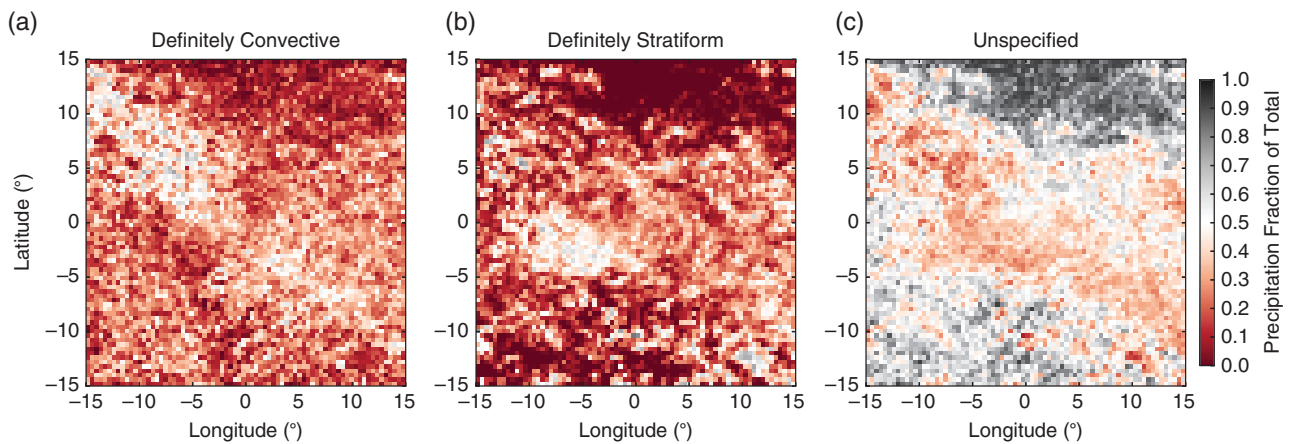

Figure 9. Composite rain fraction computed using objective rain type from *TRMM* 2A23 and estimated surface rain rate from *TRMM* 2A25. (a) Convective; (b) stratiform; (c) events not attributable to the previous two categories. See text for a definition of 'definitely'.

peninsula. There is an arguably greater propensity for convective precipitation in the northwest, as the MD starts to push into the drier desert environment of Pakistan; there is significant area of more likely stratiform precipitation southwest of the centre, a little further out than the location of the precipitation maximum.

Figure 10 shows the composite proportion of surface precipitation that is at least maybe attributable to convective and stratiform systems, again with the remainder on the right. This time, almost all rainfall events have been assigned a type, bar a handful of outliers. This looks much like an amplification
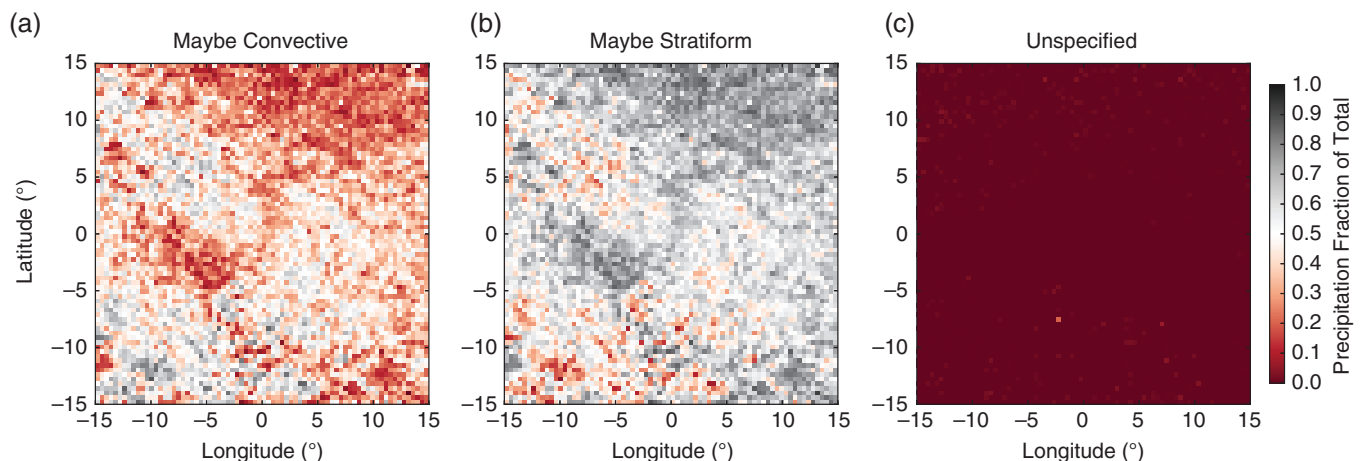

Figure 10. As Figure 9, but using a 'maybe' threshold (i.e. up to and including 'definitely'). (a) Convective; (b) stratiform; (c) events not attributable to the previous two categories.
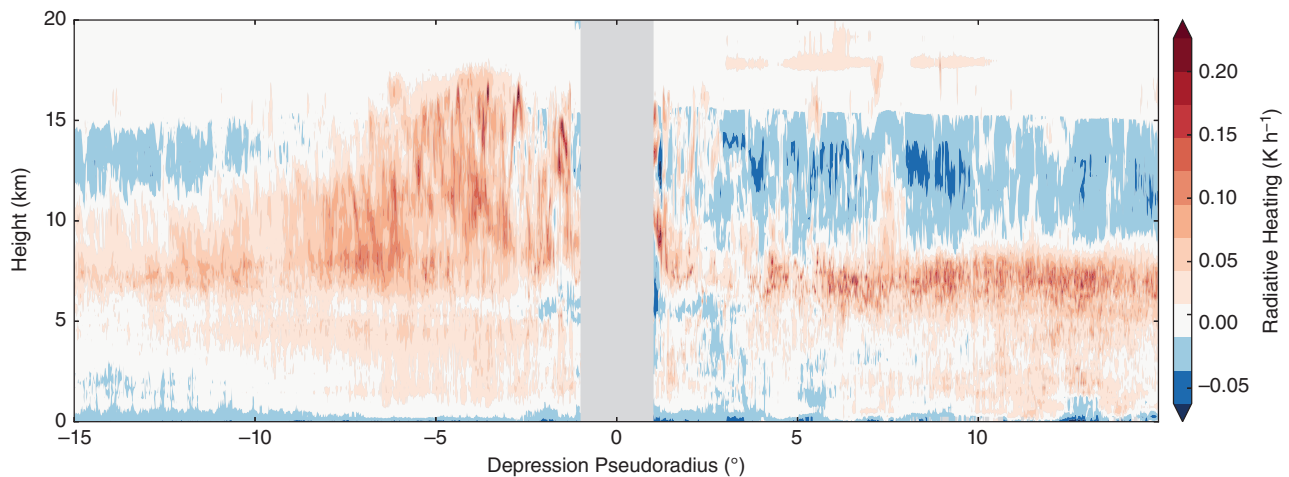
Figure 11. Composite vertical radiative heating profile (K h^{-1}) within the MD from both long-wave and short-wave radiation, derived from *CloudSat* 2B-FLXHR. Data removed as per Figure 5.

of the signals in Figure 9, except that the rainfall over/around the Himalayas has mostly been designated as stratiform (as we would expect). It is not obvious why we see the high ($\sim$ 50% definite, $\sim$ 80% maybe) stratiform allocation covering a significant area approximately 500 km southwest of the centre, as we might expect this to be quite convective. Given that the stratiform allocation relies strongly on bright band detection and we know one can exist there, even in the clearly convective regime closer to the centre (cf. Figures 4 and 5), this could be tricking the algorithm into the wrong diagnosis. Houze (1997) discussed this apparent problem in some detail, but it is clear we should interpret the results displayed in Figures 9 and 10 with due caution.

3.3. Diabatic heating: latent and radiative

Whilst much of the thermodynamics in the atmosphere are dominated by adiabatic processes, in the tropics, and particularly in cyclonic tropical systems where precipitation and cloud cover are appreciably increased, we must also consider diabatic processes in order to form a complete picture. MDs have dense cloud cover at all levels (Godbole, 1977; Hunt *et al.*, 2016), resulting in complicated radiative heating/cooling profiles, which, in this study, we will attempt to demonstrate. Further, the constant flux and phase changing of atmospheric moisture in MDs results in widespread latent heating/cooling. By far the most most important phase transition in MDs is lower-tropospheric condensation of warm, water-vapour laden air rising from near the surface (with a secondary contribution from freezing in the mid-troposphere). It has long been proposed that this latent heat release is intrinsic to conditional instability of the second kind and is a potential source of energy for MDs moving over the ocean (Shukla, 1978). The *CloudSat*-derived radiative heating profile is shown in Figure 11 and looks as we might naively expect from inspection of the cloud cover in Figure 6: substantial short-wave heating at and slightly beneath the cloud tops (particularly the thicker convective clouds) and long-wave cooling elsewhere. The composite heating rates in the upper troposphere south of the centre can reach over 0.2 K h^{-1}; this value is more than an order of magnitude less than what one might expect at the top of a tropical anvil (Ackerman *et al.*, 1988), but still considerably more than the summer monsoon climatology (not shown). The small magnitude arises because, while the MD is dominated by instances of deep convection, the cloud tops of which are strongly heated, these vary in height and precise location and are thus smoothed out in the composite. We will later evaluate this discussion in the context of a case study, in particular diagnosing the features of a large anvil structure.

We can use data from *TRMM* to inspect the composite latent heating profile, which is given in Figure 12. This figure also shows two 1D profiles through selected pseudoradii. We can instantly deduce that latent heating is the larger of the two diabatic heat sources in MDs, as it is in the tropics in general (Roca *et al.*, 2010): the intense convective rain south of centre leads to a composite mean latent heating rate of as much as 1.8 K h^{-1} in the mid-troposphere, supporting the warm core found there in other studies (e.g. Godbole, 1977, and many others).

3.4. Reanalysis composite

We can use ERA-Interim reanalysis data to construct a few more useful composites and complete our discussion. Figure 13 shows the structures of (a) temperature anomaly, (b) vertical velocity and (c) divergence, respectively, and we can use these to develop the ideas introduced in this section so far. These reanalysis composites are constructed in the same way as those previously derived from satellite data in this study. The similarity of all three panels to those computed from the full three-dimensional composite technique used for MDs in Hunt *et al.* (2016) is a useful indicator that the pseudoradial method used here is robust. Summarizing briefly, we have found that the region of maximum rainfall in MDs is collocated with a significant area of deep convection and intense low-tropospheric latent heating rates. There is no clear significant cloud structure to the north of the depression, other than the presence of orographically induced stratus, which are also associated with increased rainfall.

Figure 13(a) shows the composite vertical temperature structure, taken as an anomaly to the June−September summer climatology. It bears some horizontal resemblance to the two diabatic heating fields discussed in the previous section, but this semblance is lost in the vertical. Monsoon depressions are roughly in thermal wind balance, so we should not expect to be able to explain the gross thermal structure in terms of local heating rates (especially radiative); however, it is not implausible that the strong latent heating in the lower middle troposphere warms air that is subsequently lifted by the deep convection in which it generally sits.

Figure 13(b) shows vertical velocity; this is provided by ERA-Interim as ω ($= \partial P/\partial t$) and has been converted to w ($= \partial h/\partial t$) here for convenience. There is a fairly strong similarity between this field and the observed cloud-cover structure shown in Figure 6, indicating (as expected) that much of this cloud is convective; we can support this assertion further by noting that the maximum upward speed in the lower troposphere is collocated with the maximum rainfall rates (see Figure 2) at each height. Finally, in Figure 13(c), a composite of divergence is shown. Given the results so far and in particular bearing in mind the theory suggested by Yoon and Chen (2005) that
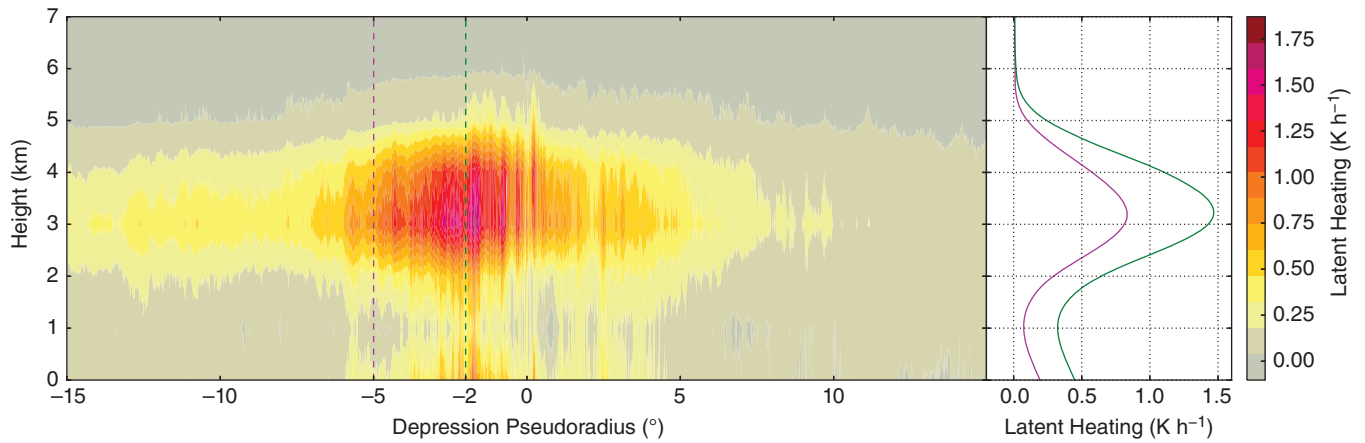
Figure 12. Left: Composite vertical latent heating profile (K h^{-1}) from hydrometeor fluxes within the MD as a function of pseudoradius, derived from *TRMM* 2B31. Right: Two selected vertical profiles from the composite, $-5°$ (magenta) and $-2°$ (green). Note the short vertical axis due to negligible mean latent heating rate above the freezing level.
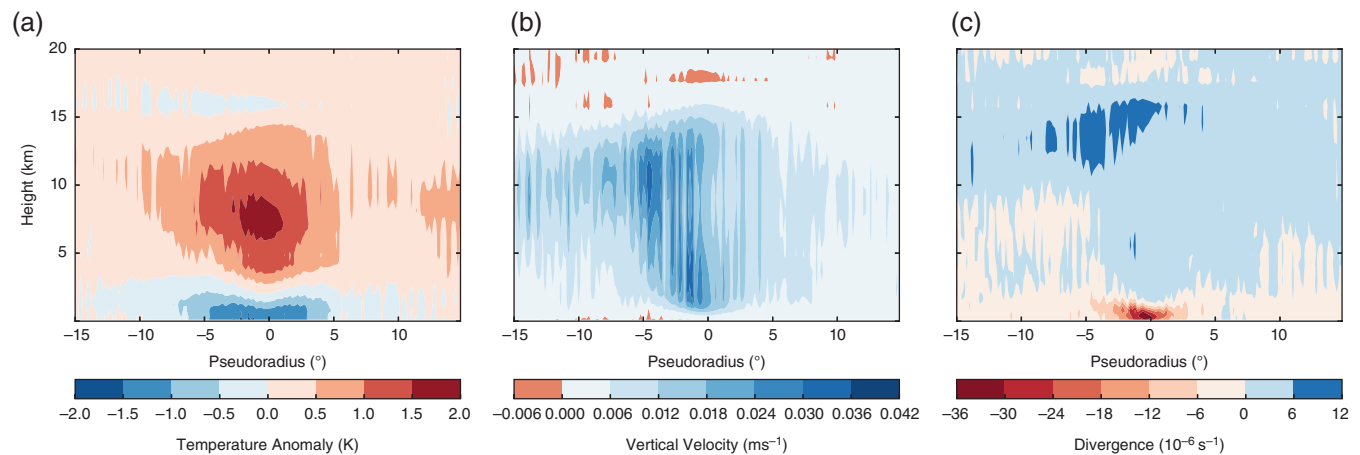

Figure 13. Several composite variables as functions of pseudoradii and height. (a) Temperature (K) as an anomaly to the boreal summer mean, (b) vertical velocity (m s^{-1}, positive upwards), (c) divergence (10^{-6} s^{-1}). Data are from ERA-Interim reanalysis for the composite.

the rainfall asymmetry in a depression is controlled by low-level moisture convergence modulated by larger-scale monsoon variability, the fact that the rainfall and convergence maxima are not collocated is perhaps surprising. Given that the gradient of specific humidity across the depression is not steep enough to shift the moisture flux convergence maximum far from the air convergence maximum, moisture convergence is not the mechanism responsible for the asymmetry, in accord with the moisture trajectory analysis of Hunt *et al.* (2016), who found that the dominant moisture flux convergence terms in MDs were slightly asymmetrical but not off-centre enough to explain the precipitation maximum correctly. Recalling, then, the three suggested theories for the precipitation southwest maximum in Mooley (1973), we can now rule out the hypothesis that the asymmetry is caused by an off-centre moisture-flux convergence maximum. Further, inspection of Figure 6 very strongly suggests that this phenomenon is not due to the westward axial tilt observed in some fields of the MD with height. Ruling these out leaves us with the hypothesis that this activity peaks southwest of the centre due to the cyclonic mixing (and subsequent forced ascent) of warm, humid air from the Arabian Sea with the cooler, drier, continental air mass. If this is correct, this feature would be unique to the monsoon depressions of India; unfortunately, a detailed study of rainfall in global monsoon depressions has not yet been carried out, but some case-study analysis of Australian monsoon depressions by Zhao and Mills (1991) and a more recent study by Berry *et al.* (2012) of objectively tracked Australian monsoon disturbances suggest that this is indeed the case.

4. Case study

The nature of this research prompts a validation of the satellite products, both with each other and with independent data. For this purpose, we carry out a case study, which benefits us further with some validation of the composite discussed previously. We select an event where *TRMM* and *CloudSat* overpasses intersect near an MD centre within a short time frame. The best such example was the MD of early July 2007; see Figure 14: the overpass intersection was separated by 62 minutes at a distance of just 96 km from the depression centre. This figure also shows the locations of the sixteen gauge sites used for *TRMM* validation later in this section, as well as the total accumulated rainfall (if > 20 mm) for the UTC day 7 July 2007, for which the depression started on the yellow marker and progressed westward by four markers. This shows well the propensity for an MD rainfall maximum to be southwest of the centre, which is in fact where almost all the heavy rainfall is; recall that the central India average daily rainfall in July is approximately 10 mm day^{-1} and so even the *lowest* contour here is twice that value. Note also the presence of an unrelated storm over northeast India and the coastal rainfall associated with southeast Asia, as well as significantly enhanced rainfall over the Western Ghats as a result of the MD enhancing westerlies there. This pattern agrees with Hunt *et al.* (2016), who found that depressions result in enhanced rainfall along the Western Ghats and along the coast of southeast Asia (among other areas).

The July 2007 event was a fairly typical MD in terms of duration, trajectory, genesis and dissipation (Hurley and Boos, 2015; Hunt and Parker, 2016): spending some spin-up time at the head of
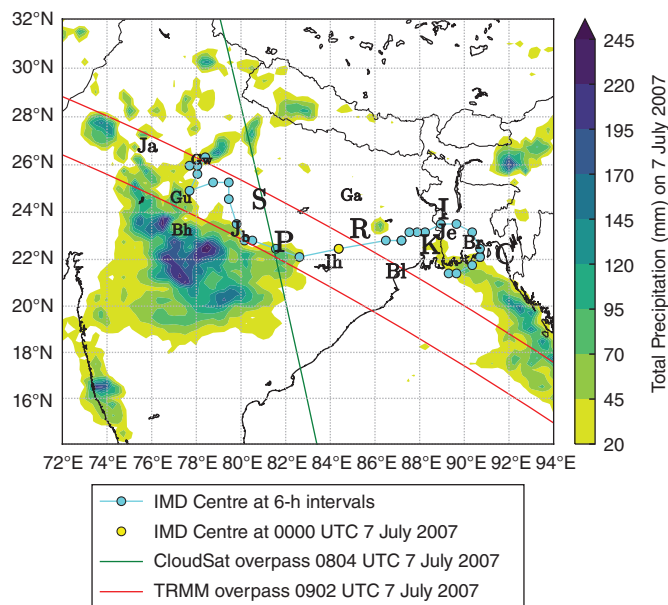
Figure 14. Path of the early July 2007 MD: six-hourly intervals plotted in cyan markers, with the location at 0000 UTC on 7 July in yellow. The areas covered by the *TRMM* and *CloudSat* overpasses are bounded by red and green lines, respectively. The locations of the 16 rain-gauges used in the rainfall comparison are also shown, West to east, they are Jaipur (Ja), Guna (Gu), Bhopal (Bh), Gwalior (Gw), Jabalpur (Jb), Satna (S), Pendra Road (P), Jharsuguda (Jh), Gaya (Ga), Ranchi (R), Balasore (Bl), Kolkata (K), Ishwardi (I), Jessore (Je), Barisal (Br) and Chittagong (C). Overlaid (coloured contours, mm) is the total precipitation for the UTC day 7 July.

the Bay of Bengal before making landfall in Bangladesh/northeast India, propagating parallel to the Himalayas before dissipating over northwest India. This makes it a good candidate for this case study, in that there is nothing unusual we should be aware of. We now have an idea of the basic footprint of this particular MD and are in a position to look at the respective *TRMM* and *CloudSat* overpasses. Selected data from each are shown in Figure 15, with *TRMM* in the top three panels, *CloudSat* in the next three and ERA-Interim (following the *CloudSat* trajectory, but approximately 3 h earlier). Each panel is directly analogous to a figure discussed in the previous section, with the exception of the third-from-bottom subfigure, which shows the reflectivity (dBZ) measured by *CloudSat*. For each satellite, the data are represented as projections on to the longest global coordinate axis for the overpass in question: latitude for the polar-orbiting *CloudSat* and longitude for the 35° inclination *TRMM*. Since *TRMM* data are from finite-width swaths, these are meridionally averaged before projection. The location of the centre of the depression at the time of the overpasses was 22.5°N, 81.6°E, and these values on their respective axes in Figure 15 should be taken as such – they are marked with a 'C'. Both overpasses indicate that there is some activity directly over the centre, but that there is more intense activity several hundred kilometres away (distinct for each overpass). The data from *CloudSat* indicate that the centre sits under the edge of a very large anvil cloud, the shape of which is well captured; large radiative heating across the top and a strong (subsequently attenuated) reflectivity indicate the presence of dense, tall cloud here. There is also evidence of some activity in the north too, with stratiform and orographic cloud present around the Himalayas. The *TRMM* overpass was slightly less fortunate with positioning, but still captured some interesting features: a convective bloom approximately 500 km to the west of the depression, some activity associated with the centre and an area to its north, and the coastal rainfall of southeast Asia. All three areas demonstrate convective activity, but the area north of the MD centre has the weakest: we might expect this, given the previous analysis, but even so, there are rainfall rates here of up to 10 mm h^{-1} driving latent heating of the order of 10 K h^{-1}.

We cannot say with certainty that the deepest convection (in the northwest) is necessarily associated with the depression, but inspection of Figure 14 suggests that it is probable.

The inclusion of some almost contemporaneous ERA-Interim data, nearest-neighbour-interpolated to the *CloudSat* ground track, permits us to make some general comments on the thermodynamical interpretation of these fields. Firstly, we must note that ERA-Interim has a fairly coarse spatial and temporal resolution: the latter constraint requires us to choose the 1200Z fields, nearly three hours after the relevant *CloudSat* overpass; this discrepancy will cause some apparent displacement when comparing fields from both. Secondly, we also note that the temperature field is taken as an anomaly to the June–September climatology, computed on a grid point by grid point basis. In both reanalysis fields presented in Figure 15, the form quite closely resembles the gross composite structure computed by Hunt *et al.* (2016); however, there are also some distinctive features to remark upon.

With some confidence, we can associate the strong vertical lifting at approximately 22°N with the deepest convection, but we also note that much of that same anvil is collocated with lifting confined to the lower troposphere and is flanked by large areas of upper/mid-tropospheric subsidence that appear to be suppressing convection; there is also a deep anomalously warm core aloft with large spatial extent, overlapping both the deep convection and the surrounding area of descent. The large spatial extent of the depression – examination of the anomalous zonal wind (not shown) indicates that 10 m s^{-1} isosurfaces reach beyond the 15th and 30th parallels – makes it highly plausible that the anomalous ascent at the Himalayan foothills and resulting cloud structure there are also directly related to the circulation of the MD.

The individuality of this MD shows that the results of section 2.2 should be treated as a composite, not a 'mean-state' depression, as can be done for less spatially variable fields (Hunt *et al.*, 2016). We can, however, create a composite representation showing the mean when the field is non-zero alongside the probability that that is the case (e.g. the mean rain rate when there is rain and the overall probability of rain for that location). If we do this, we find two things: firstly, that the shape is very similar, with the small exception of a more prominent local extremum at the centre; secondly, the magnitude of all hydrometeor and diabatic heating fields is roughly doubled. The first point supports usage of the composite in the form given throughout this study, as the main source of structure in it is the magnitude of the fields, not the probability of activity at that location.

Now that we have an instantaneous snapshot of this depression, we can further our understanding by examining how its passage affects the atmosphere around it using observational data. Such analysis is fairly rife in literature on a case study by case study or small composite basis (e.g. Koteswaram and George, 1960; Krishnamurti *et al.*, 1975, 1976; Daggupaty and Sikka, 1977; Godbole, 1977) and aids understanding of the dynamics involved. The MD in question passed almost directly over a sounding station at Ranchi (see Figure 14), for which daily soundings are observed at 0000 UTC. Tephigrams presenting these data are displayed in Figure 16. As expected, they show a typically warm, moist, tropical atmospheric profile with strong vertical wind shear. As the MD passes overhead, the winds strengthen and moisture is carried a lot higher in the troposphere – the entire profile is almost saturated – and significant instabilities have developed, evidenced by the numerous inversions throughout.[†] Note that the superadiabatic layer between 850 and 800 hPa in Figure 16(b) is likely specious and an instrument error. The sounding from

---

[†]The humidity (and to a lesser extent, temperature) sensors used in standard soundings generally used by the IMD have a fairly slow response, so it is important to note that the shape of the profile could be an artefact of the sensor becoming wet as it passes through multiple cloud layers. However, if this were a common issue, we would expect many soundings from the area to appear structurally similar and in general this is not the case.
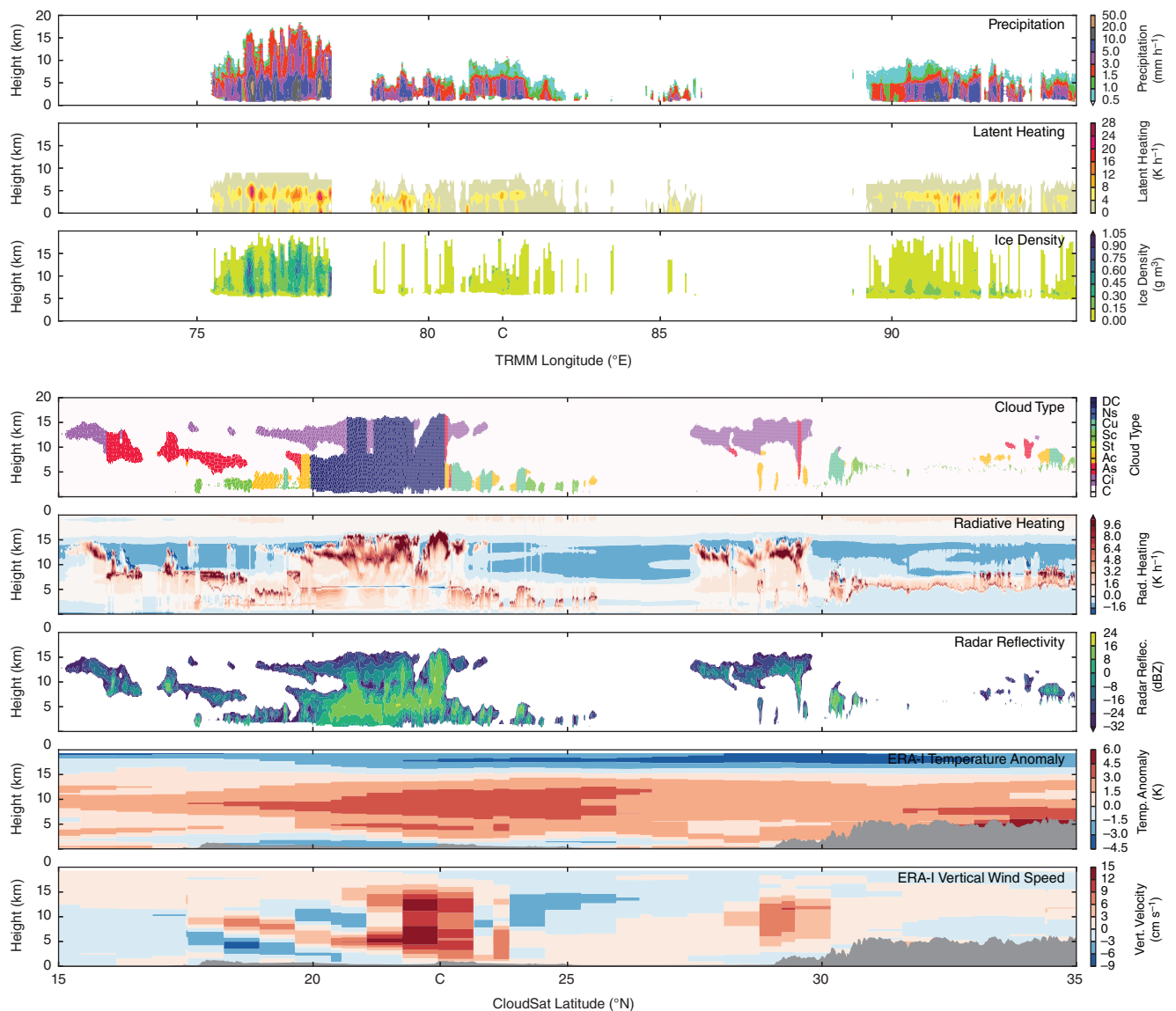
ⓒ 2016 The Authors. *Quarterly Journal of the Royal Meteorological Society* published by John Wiley & Sons Ltd on behalf of the Royal Meteorological Society.

Q. J. R. Meteorol. Soc. (2016)

Figure 15. Selected data from the *TRMM* and *CloudSat* overpasses designated in Figure 14; the bottom two panels are 12Z ERA-Interim data taken as close as possible to the *CloudSat* overpass path. 'C' on each abscissa marks the location of the centre of the depression at the time of the overpass. Where ERA-I data would be subterranean, they are greyed out.

the morning after the MD passed overhead (July 8) possesses the strongest winds (agreeing with the composite in Hunt *et al.*, 2016), but is also several degrees warmer, since the moisture packed into the column during the previous day rains out and the thick cloud clears.

We conclude this section with a brief validation of the *TRMM* 3B42 surface rainfall product against some station gauge data. This will, in general, help validate the composite image developed by providing some assurance that the presence of the depression does not cause *TRMM* to misestimate the rainfall wildly. Such evaluation has been covered in much greater detail for tropical cyclones by Chen *et al.* (2013) and over orography by Dinku *et al.* (2007, 2008, 2010); the former found that *TRMM* underestimated rainfall in tropical cyclones, particularly over land or near orography, the latter found that *TRMM* performed well over most orography, but with decreasing skill as the topography became more complex. For our evaluation, we will consider the mean and variance of both *TRMM* 3B42 and gauge-measured rainfall at the 16 stations presented in Figure 14 over the first half of July 2007. To use *TRMM* to estimate the daily rainfall accumulated at each station (reproducing the daily gauge data), we took the appropriate pixel ($0.25° \times 0.25°$) from *TRMM* 3B42 and averaged over the eight relevant three-hourly values. This and the gauge rainfall are shown in Figure 17. Further, as not all stations reported rainfall (zero or otherwise) on all days,

the equivalent data were also masked in *TRMM*. Assuming the gauge data are true, the pattern and variance is captured well by *TRMM*, however the magnitude is underestimated by as much as 30% on average during the most intense rainfall. This value is in close agreement with that found by Pokhrel and Sikka (2013) for gridded *TRMM* PR values over the whole peninsula and surrounding ocean. The data from a selection of individual stations along the MD path are presented in Figure 18; they show both the clear westward propagation of the system and the consistency of rainfall underestimation by *TRMM*.

5. Diurnal variability

It is well known that the day–night cycle drives marked changes in the atmosphere and it is reasonable therefore to surmise that there will be some diurnal cycle in the thermodynamics of MDs. The better we can quantify this finer-scale variability, the more we can design our NWP models to provide higher quality forecasts. Yet, surprisingly, discussion on the diurnal variability of MDs is almost non-existent in the literature. Hunt *et al.* (2016) showed that there is a significant contrast between depressions during the day and at night: during the day, MDs are warmer and drier throughout, with a sizeable reduction in low-level cloud cover at the centre.
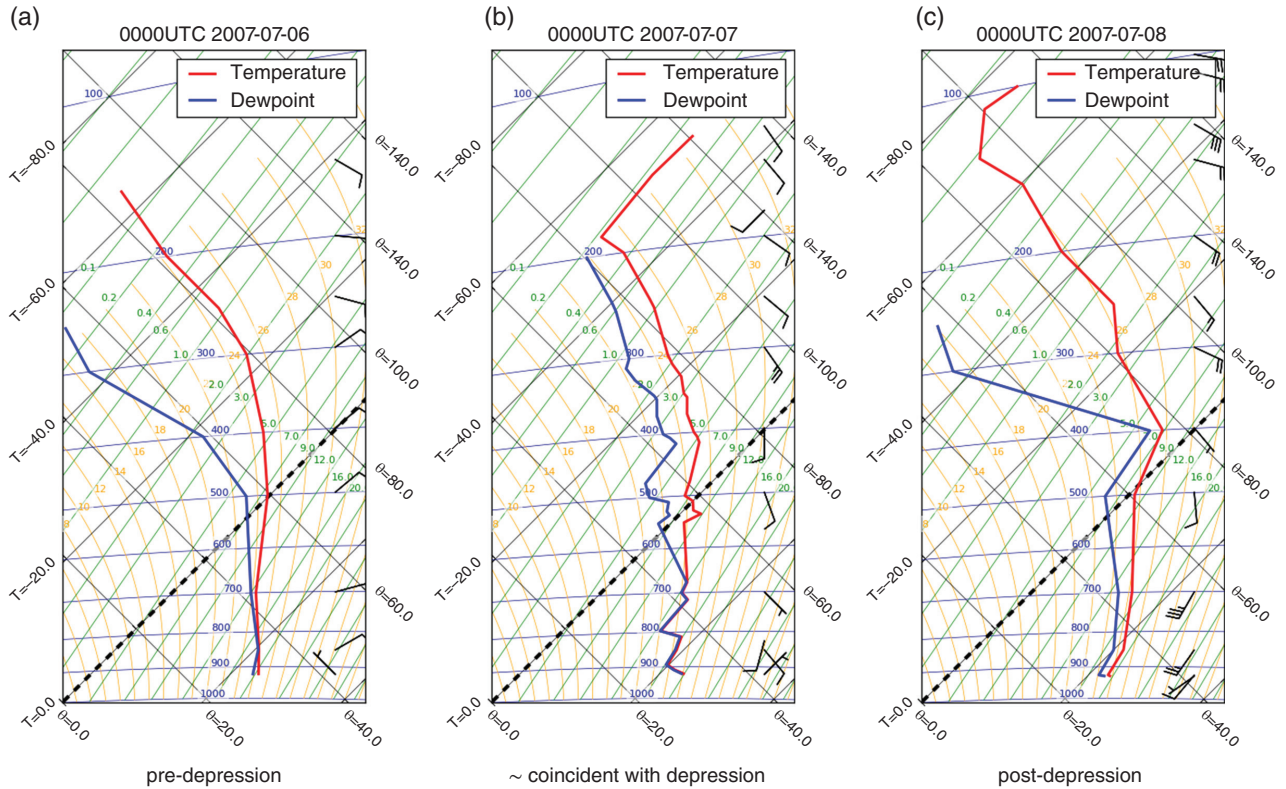
(a)

0000UTC 2007-07-06

pre-depression

(b)

0000UTC 2007-07-07

~ coincident with depression

(c)

0000UTC 2007-07-08

post-depression

Figure 16. (a–c) Tephigrams for soundings from three consecutive days at Ranchi station (see Figure 14). Red and blue lines show temperature (K) and dew-point (K) profiles, respectively, and on the right of each tephigram the wind barbs (m s^{-1}) are shown in black. Where ERA-Interim data would be below the surface, they are greyed out.
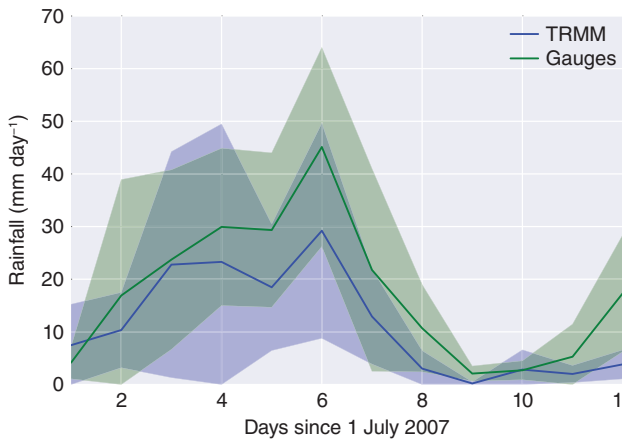

Figure 17. Comparison of the average daily precipitation (mm day^{-1}) recorded at the 16 stations shown in Figure 14 during the depression of early July 2007. Gauge values are given in green, *TRMM* 3B42 estimates are given in blue. Each is shown with a 1σ band. Where gauge measurements were missing, *TRMM* data were also omitted from the average.

Recently Bowman and Fowler (2015) used surface rainfall data from *TRMM* 3B42 to perform a detailed investigation the diurnal cycle of precipitation in a global catalogue of tropical cyclones (IBTrACS, Knapp *et al.*, 2010). They found the amplitude to vary unimodally over the diurnal cycle, with a maximum 7% greater than the mean centred at approximately 0600 local time. We are now in a position to repeat this analysis for the composite MD, as shown in Figure 19. This is performed on the rotated composite, because this filters out the diurnally varying land/sea-breeze related coastal rainfall contribution from southeast Asia. The most immediate feature in Figure 19 is the diurnal cycle of the central maximum, which has a peak at 0000 UTC (0530 IST[‡]). The

[‡]Indian Standard Time

surrounding rainfall also varies diurnally, but out of phase with the central maximum, similarly to the land–ocean contrast in the cycles displayed by the rain resulting from tropical convection (Nesbitt and Zipser, 2003; Kikuchi and Wang, 2008).

The thermodynamics behind both types of diurnal cycle are already well understood. Tropical convective precipitation peaks in the late afternoon as the result of a number of coupled processes, but can be thought of most simply as cumulative surface heating from insolation generating maxima in sensible and latent surface heat fluxes, promoting static destabilization (e.g. Byers and Braham, 1948; Ogura and Takahashi, 1971; Bechtold *et al.*, 2004; Hirose and Nakamura, 2005). In contrast, the diurnal cycle of tropical cyclone precipitation is a result of the enhanced nocturnal radiative cooling of anvil cloud tops destabilizing the upper troposphere (e.g. Kraus, 1963; Tripoli, 1992), an effect with magnitude peaking around local dawn.

We propose that these fields can be simply modelled by fitting a sum of two arbitrarily phased two-dimensional Gaussian functions with some climatological offset (or residual), of the form

$$P(x, y) = P_{\text{residual}}(x, y)$$

$$+ \sum_{n=0}^{1} A_n \exp\left(-\begin{bmatrix} x - x_{o,n} & y - y_{o,n} \end{bmatrix} \right.$$

$$\left. \begin{bmatrix} \dfrac{\cos^2\theta_n}{2\sigma_{x,n}^2} + \dfrac{\sin^2\theta_n}{2\sigma_{y,n}^2} & \dfrac{\sin 2\theta_n}{4\sigma_{x,n}^2} - \dfrac{\sin 2\theta_n}{4\sigma_{y,n}^2} \\ \dfrac{\sin 2\theta_n}{4\sigma_{x,n}^2} - \dfrac{\sin 2\theta_n}{4\sigma_{y,n}^2} & \dfrac{\sin^2\theta_n}{2\sigma_{x,n}^2} + \dfrac{\cos^2\theta_n}{2\sigma_{y,n}^2} \end{bmatrix} \begin{bmatrix} x - x_{o,n} \\ y - y_{o,n} \end{bmatrix} \right), \quad (1)$$

where P is the observed spatial distribution of the precipitation, P_{residual} is the difference between the observed rainfall and the fitted function, n is an index for the two Gaussian functions, σ_x and σ_y refer to the standard deviation of the Gaussian along the x and y axes respectively, (x_o, y_o) are the coordinates of the centre of the Gaussian and θ is its rotational phase. We can fit these parameters to our rotated (Catto *et al.*, 2010; Hunt *et al.*,
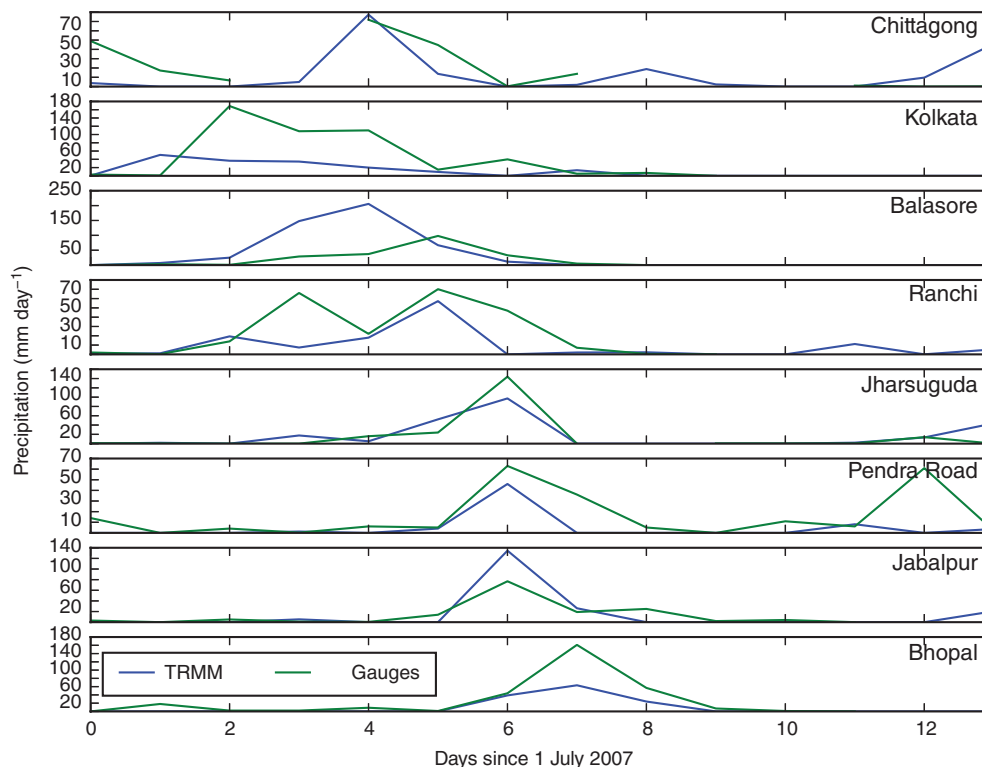
Figure 18. Daily precipitation (mm day^{-1}) for eight selected stations along the path of the depression in early July 2007, approximately from east to west. Gauge values are given in green, *TRMM* 3B42 estimates are given in blue.

2016) data using the Levenberg–Marquadt algorithm (Levenberg, 1944; Marquadt, 1963), which interpolates between the gradient-descent and Gauss–Newton methods and is a common algorithm for least-squares curve fitting. Although rotation smooths the precipitation pattern (reducing derived intensities, see Figure 1), there is no significant dependence of MD propagation direction on the time of day, so calculations of the relative diurnal cycle will not be affected. Performing this analysis on the rotated composite yields a stable convergence for the fitting algorithm and a robust final fit; indeed, we recover both modes of the diurnal cycle (Figure 20). The distribution given by this fitted function passes a Pearson's chi-squared goodness-of-fit test at a 95% confidence interval when compared with the observations.

It is evident that the two modes are very much in antiphase and that the central mode is always responsible for the more intense rainfall: it has a mean value of 25.0 mm day^{-1} compared with 12.1 mm day^{-1} for the outer mode. However, both modes have a similar variability: 70% and 64% peak-to-trough for the central and outer modes, respectively. These values are markedly larger than that quoted by Bowman and Fowler (2015) for tropical cyclones, because we are considering two distinct modes varying in antiphase, but even if we only fit one Gaussian across the cycle we still recover a diurnal cycle with peak-to-trough variability of 36% and a maximum at 0000 UTC. We have shown, therefore, that MDs exhibit substantially greater diurnal variability in surface rainfall than tropical cyclones and that there are two main processes responsible for this precipitation. Further work is needed to determine to what extent these modes are coupled.

Analysis of the unrotated composite by empirical orthogonal function (EOF) decomposition shows that the diurnal cycle discussed here is the principal mode of variability; the second most dominant mode manifests as an east–west translation of the location of maximum rainfall that also varies on a diurnal cycle: eastmost at 0000 UTC, westmost at 1200 UTC. This could be due to the zonal gradient of heat flux from the ground as maximum insolation moves westward throughout the day, or some more complicated Rossby-wave dynamics via land–sea thermal contrast.

6. Conclusions

Indian monsoon depressions are relatively long-lived tropical lows that usually cross central India several times each summer. They are exceptionally moist synoptic-scale systems that often increase precipitation in north and central India drastically during their passage across the subcontinent. A description of the precipitating processes and moist thermodynamics of MDs is therefore important for scientific understanding and the evaluation of climate models and NWPs, so that their potential impact on the urban and agrarian cultures in flood-susceptible areas can be better constrained. The method presented here provides a basis whereby MDs in NWP models and GCMs can also be composited and subsequently evaluated.

This is the first such detailed study to use satellite data to bring forward a composite image of these processes and therefore it provides a number of novel results to this field. We have confirmed the long-known presence of a surface rainfall maximum several hundred kilometres southwest of the centre and attributed it to collocated deep convection. We have shown that this area of convection is substantial, both in the composite and in a case study, extending for upwards of 500 km from near the centre towards the south(west). We have also shown that the hydrometeor structure is far less symmetric than previously assumed: rain to the north of the centre is up to an order of magnitude less than can be found at the same radius to the south of the centre and deep convection is entirely absent as a significant process in the north: almost all precipitation is stratiform, driven by interaction with the orography of the Himalayan foothills.

We have shown that MDs have consistently deep convection collocated with the area of maximum precipitation, covering a significant region. Within this, the highest raindrop density is found, directly beneath the highest densities of snow and graupel. The largest raindrops, however, are found at the centre, where, in the comparatively uncommon event of convection occurring, the highest rainfall rates can also be found. Outside the centre, the raindrop size distributions tend to be uniform with height up to about 5 km, implying that these areas are well mixed. To the south of this deep convection, we have shown the cloud structure
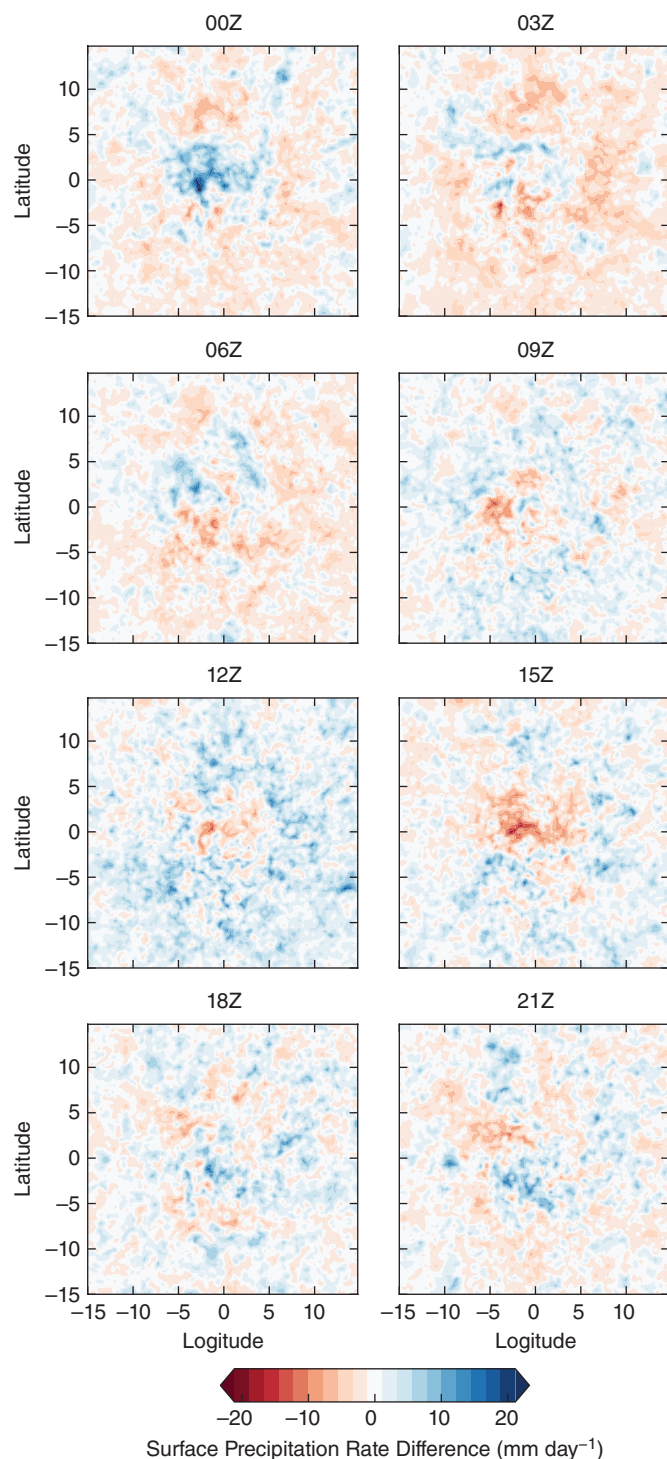
Figure 20. Amplitudes of the two diurnal modes of surface precipitation (mm day^{-1}) in the rotated composite, derived from *TRMM* 3B42.

variation 64%). A full understanding of these dynamical features will require detailed regional simulations with high-resolution models.

Further work is now needed to look at the mechanisms responsible for the decay and ultimate dissipation of depressions and investigate what is responsible for the zonal shift of the precipitation maximum across the diurnal cycle and how convection parameters in numerical models affect their propagation and duration.

Acknowledgements

References

Ackerman TP, Liou KN, Valero FP, Pfister L. 1988. Heating rates in tropical anvils. *J. Atmos. Sci.* **45**: 1606–1623.

Awaka J, Iguchi T, Kumagai H, Okamoto K. 1997. 'Rain type classification algorithm for *TRMM* precipitation radar'. In *Geoscience and Remote Sensing, 1997: IGARSS'97, Remote Sensing – A Scientific Vision for Sustainable Development*, Vol. 4. Institute of Electrical and Electronics Engineers: New York, NY, pp. 1633–1635.

Awaka J, Iguchi T, Okamoto K. 2007. Rain type classification algorithm. In *Measuring Precipitation From Space: EURAINSAT and the Future*, Levizzani V, Bauer P, Turk FJ (eds.), 213–224, Springer: Houten, The Netherlands.

Bechtold P, Chaboureau JP, Beljaars A, Betts A, Köhler M, Miller M, Redelsperger JL. 2004. The simulation of the diurnal cycle of convective precipitation over land in a global model. *Q. J. R. Meteorol. Soc.* **130**: 3119–3137.

Berry GJ, Reeder MJ, Jakob C. 2012. Coherent synoptic disturbances in the Australian monsoon. *J. Clim.* **25**: 8409–8421.

Bowman KP, Fowler MD. 2015. The diurnal cycle of precipitation in tropical cyclones. *J. Clim.* **28**: 5325–5334, doi: 10.1175/JCLI-D-14-00804.1.

Byers HR, Braham RR. 1948. Thunderstorm structure and circulation. *J. Meteorol.* **5**: 71–86.

Catto JL, Shaffrey LC, Hodges KI. 2010. Can climate models capture the structure of extratropical cyclones? *J. Clim.* **23**: 1621–1635, doi: 10.1175/2009JCLI3318.1.

Figure 19. Composite rotated structure of surface precipitation rate (mm day^{-1}) in MDs at 3 h intervals across the UTC day as anomaly to the mean, derived from *TRMM* 3B42.

to be typically tropical, whereas to the north of the centre it is far more orographically driven.

Our case study shows that the presence of an MD sets up multiple instabilities in the atmosphere and saturates the troposphere up to 600 hPa. Using this example, we also compared *TRMM*-based surface rainfall estimates with station gauge-based estimates along the MD track, finding that *TRMM* 3B42 can significantly underestimate the higher rainfall rates associated with MDs: the highest rainfall rates were underpredicted by 30%.

We discovered and quantified a bimodal diurnal rainfall cycle in MDs: an uncoupled, antiphase cycle with a central mode (associated with the maximum precipitation in the southwest, peak-to peak variation 70%) and an outer mode (associated with the general convective precipitation across the MD, peak-to-peak
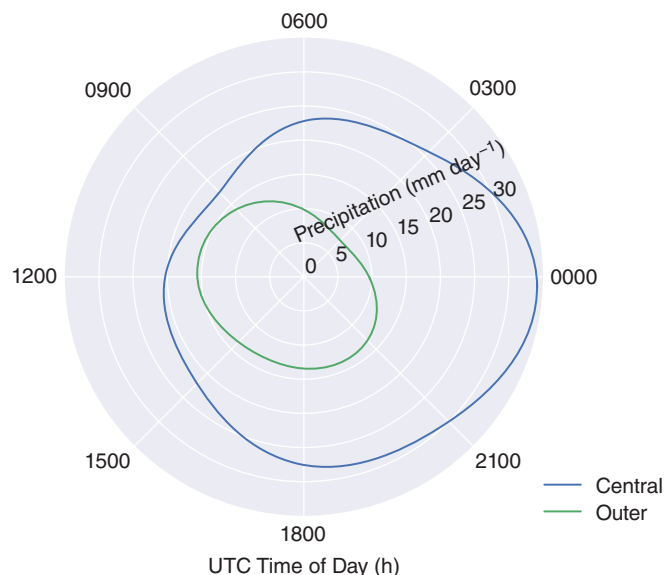
Chen Y, Ebert EE, Walsh KJ, Davidson NE. 2013. Evaluation of *TRMM* 3B42 precipitation estimates of tropical cyclone rainfall using PACRAIN data. *J. Geophys. Res. Atmos.* **118**: 2184–2196, doi: 10.1002/jgrd.50250.

Daggupaty SM, Sikka DR. 1977. On the vorticity budget and vertical velocity distribution associated with the life cycle of a monsoon depression. *J. Atmos. Sci.* **34**: 773–792.

Dee DP, Uppala SM, Simmons AJ, Berrisford P, Poli P, Kobayashi S, Andrae U, Balmaseda MA, Balsamo G, Bauer P, Bechtold P, Beljaars ACM, van de Berg L, Bidlot J, Bormann N, Delsol C, Dragani R, Fuentes M, Geer AJ, Haimberger L, Healy SB, Hersbach H, Hólm EV, Isaksen L, Kållberg P, Köhler M, Matricardi M, McNally AP, Monge-Sanz BM, Morcrette JJ, Park BK, Peubey C, de Rosnay P, Tavolato C, Thépaut JN, Vitart F. 2011. The ERA-Interim reanalysis: Configuration and performance of the data assimilation system. *Q. J. R. Meteorol. Soc.* **137**: 553–597, doi: 10.1002/qj.828.

Desai BN. 1951. On the development and structure of monsoon depressions in India. *Mem. India Meteorol. Dept.* **28**: 217–228.

Dinku T, Ceccato P, Grover-Kopec E, Lemma M, Connor S, Ropelewski C. 2007. Validation of satellite rainfall products over East Africa's complex topography. *Int. J. Remote Sens.* **28**: 1503–1526.

Dinku T, Chidzambwa S, Ceccato P, Connor S, Ropelewski C. 2008. Validation of high-resolution satellite rainfall products over complex terrain. *Int. J. Remote Sens.* **29**: 4097–4110.

Dinku T, Connor SJ, Ceccato P. 2010. Comparison of CMORPH and *TRMM*-3B42 over mountainous regions of Africa and South America. In *Satellite Rainfall Applications for Surface Hydrology*: 193–204. Springer: The Netherlands.

Fu Y, Liu G. 2001. The variability of tropical precipitation profiles and its impact on microwave brightness temperatures as inferred from *TRMM* data. *J. Appl. Meteor.* **40**: 2130–2143, doi: 10.1175/1520-0450(2001)040<2130:TVOTPP>2.0.CO;2.

Godbole R. 1977. The composite structure of the monsoon depression. *Tellus* **29**: 25–40.

Haddad ZS, Short D, Durden SL, Im E, Hensley S, Grable MB, Black R. 1997a. A new parametrization of the rain drop size distribution. *IEEE Geosci. Remote Sens. Lett.* **35**: 532–539.

Haddad ZS, Smith EA, Kummerow CD, Iguchi T, Farrar MR, Durden SL, Alves M, Olson WS. 1997b. The *TRMM* day-1 radar/radiometer combined rain-profiling algorithm. *J. Meteorol. Soc. Jpn.* **75**: 799–809.

Haynes JM, L'Ecuyer TS, Stephens GL, Miller SD, Mitrescu C, Wood NB, Tanelli S. 2009. Rainfall retrieval over the ocean with spaceborne W-band and radar. *J. Geophys. Res. Atmos. (1984–2012)* **114**: D00A22, doi: 10.1029/2008JD009973.

Hence DA, Houze RA. 2011. Vertical structure of hurricane eyewalls as seen by the *TRMM* precipitation radar. *J. Atmos. Sci.* **68**: 1637–1652.

Hirose M, Nakamura K. 2005. Spatial and diurnal variation of precipitation systems over Asia observed by the *TRMM* precipitation radar. *J. Geophys. Res. Atmos.* **110**: D05106, doi: 10.1029/2004JD004815.

Houze RA. 1997. Stratiform precipitation in regions of convection: A meteorological paradox? *Bull. Am. Meteorol. Soc.* **78**: 2179–2196.

Houze RA, Wilton DC, Smull BF. 2007. Monsoon convection in the Himalayan region as seen by the *TRMM* precipitation radar. *Q. J. R. Meteorol. Soc.* **133**: 1389–1411.

Huffman GJ. 1997. Estimates of root-mean-square random error for finite samples of estimated precipitation. *J. Appl. Meteorol.* **36**: 1191–1201.

Huffman GJ, Adler RF, Rudolf B, Schneider U, Keehn PR. 1995. Global precipitation estimates based on a technique for combining satellite-based estimates, rain-gauge analysis, and NWP model precipitation information. *J. Clim.* **8**: 1284–1295.

Huffman GJ, Adler RF, Arkin P, Chang A, Ferraro R, Gruber A, Janowiak J, McNab A, Rudolf B, Schneider U. 1997. The global precipitation climatology project (GPCP) combined precipitation dataset. *Bull. Am. Meteorol. Soc.* **78**: 5–20.

Huffman G, Bolvin D, Nelkin E, Wolff D, Adler R, Gu G, Hong Y, Bowman K, Stocker E. 2007. The *TRMM* multisatellite precipitation analysis (TMPA): Quasi-global, multiyear, combined-sensor precipitation estimates at fine scales. *J. Hydrometeorol.* **8**: 38–55, doi: 10.1175/JHM560.1.

Huffman GJ, Adler RF, Bolvin DT, Nelkin EJ. 2010. The *TRMM* multi-satellite precipitation analysis (TMPA). In *Satellite Rainfall Applications for Surface Hydrology*: 3–22. Springer: The Netherlands.

Hunt KMR, Parker DJ. 2016. The movement of Indian monsoon depressions by interaction with image vortices near the Himalayan wall. *Q. J. R. Meteorol. Soc.* **142**(698): 2224–2229, doi: 10.1002/qj.2812.

Hunt KMR, Turner AG, Inness PM, Parker DE, Levine RC. 2016. On the structure and dynamics of Indian monsoon depressions. *Mon. Weather Rev.* **144**: 3391–3416, doi: 10.1175/MWR-D-15-0138.1.

Hurley JV, Boos WR. 2015. A global climatology of monsoon low pressure system. *Q. J. R. Meteorol. Soc.* **141**: 1049–1064, doi: 10.1002/qj.2447.

Iguchi T, Kozu T, Meneghini R, Awaka J, Okamoto K. 2000. Rain-profiling algorithm for the *TRMM* precipitation radar. *J. Appl. Meteorol.* **39**: 2038–2052.

Jakob C. 1999. Cloud cover in the ECMWF reanalysis. *J. Clim.* **12**: 947–959.

Kawanishi T, Takamatsu H, Kozu T, Okamoto K, Kumagai H. 1993. 'TRMM precipitation radar'. In *Geoscience and Remote Sensing Symposium:*

IGARSS'93. Better Understanding of Earth Environment. IEEE, Kogakuin University: Shinjuku, Japan, pp. 423–425.

Kawanishi T, Kuroiwa H, Kojima M, Oikawa K, Kozu T, Kumagai H, Okamoto K, Okumura M, Nakatsuka H, Nishikawa K. 2000. *TRMM* precipitation radar. *Adv. Space Res.* **25**: 969–972.

Kikuchi K, Wang B. 2008. Diurnal precipitation regimes in the global tropics. *J. Clim.* **21**: 2680–2696, doi: 10.1175/2007JCLI2051.1.

Knapp KR, Kruk MC, Levinson DH, Diamond HJ, Neumann CJ. 2010. The international best track archive for climate stewardship (IBTrACS) unifying tropical cyclone data. *Bull. Am. Meteorol. Soc.* **91**: 363–376.

Koteswaram P, George C. 1960. A case study of a monsoon depression in the Bay of Bengal. In *Monsoons of the World*: 145–156. India Meteorological Department: New Delhi, India.

Kraus EB. 1963. The diurnal precipitation change over the sea. *J. Atmos. Sci.* **20**: 551–556.

Krishnamurthy V, Shukla J. 2007. Intraseasonal and seasonally persisting patterns of Indian monsoon rainfall. *J. Clim.* **20**: 3–20, doi: 10.1175/JCLI3981.1.

Krishnamurti T, Kanamitsu M, Godbole R, Chang C, Carr F, Chow J. 1975. Study of a monsoon depression (I): Synoptic structure. *J. Meteorol. Soc. Jpn.* **53**: 227–240.

Krishnamurti T, Kanamitsu M, Godbole R, Chang C, Carr F, Chow J. 1976. Study of a monsoon depression (II): Dynamical structure. *J. Meteorol. Soc. Jpn.* **54**: 208–225.

Kummerow C, Barnes W, Kozu T, Shiue J, Simpson J. 1998. The tropical rainfall measuring mission (*TRMM*) sensor package. *J. Atmos. Oceanic Technol.* **15**: 809–817, doi: 10.1175/1520-0426(1998)015<0809:TTRMMT>2.0.CO;2.

Kummerow C, Simpson J, Thiele O, Barnes W, Chang A, Stocker E, Adler R, Hou A, Kakar R, Wentz F, Ashcroft P, Kozu T, Hong Y, Okamoto K, Iguchi T, Kuroiwa H, Im E, Haddad Z, Huffman G, Ferrier B, Olson WS, Zipser E, Smith EA, Wilheit TT, North G, Krishnamurti T, Nakamura K. 2000. The status of the tropical rainfall measuring mission (*TRMM*) after two years in orbit. *J. Appl. Meteorol.* **39**: 1965–1982.

L'Ecuyer TS, Stephens GL. 2002. An estimation-based precipitation retrieval algorithm for attenuating radars. *J. Appl. Meteorol.* **41**: 272–285.

L'Ecuyer TS, Wood NB, Haladay T, Stephens GL, Stackhouse PW. 2008. Impact of clouds on atmospheric heating based on the R04 *CloudSat* fluxes and heating rates data set. *J. Geophys. Res. Atmos.* **113**: D00A15, doi: 10.1029/2008JD009951.

Levenberg D. 1944. A method for the solution of certain non-linear problems in least squares. *Q. Appl. Math.* **2**: 164–168.

Liu Z, Marchand R, Ackerman T. 2010. A comparison of observations in the tropical western Pacific from ground-based and satellite millimeter-wavelength cloud radars. *J. Geophys. Res. Atmos.* **115**: D24206, doi: 10.1029/2009JD013575.

Liu C, Allan RP, Brooks M, Milton S. 2014. Comparing tropical precipitation simulated by the Met Office NWP and climate models with satellite observations. *J. Appl. Meteorol. Climatol.* **53**: 200–214, doi: 10.1175/JAMC-D-13-082.1.

Marchand R, Mace GG, Ackerman T, Stephens G. 2008. Hydrometeor detection using *CloudSat* – an earth-orbiting 94-GHZ cloud radar. *J. Atmos. Oceanic Technol.* **25**: 519–533.

Marquadt D. 1963. An algorithm for least-squares estimation of nonlinear parameters. *SIAM J. Appl. Math.* **11**: 431–441, doi: 10.1137/0111030.

Mooley DA. 1973. Some aspects of Indian monsoon depressions and the associated rainfall. *Mon. Weather Rev.* **101**: 271–280.

Mull S, Rao YP. 1949. Indian tropical storms and zones of heavy rainfall. *Indian J. Phys.* **23**: 371–377.

Nesbitt SW, Zipser EJ. 2003. The diurnal cycle of rainfall and convective intensity according to three years of *TRMM* measurements. *J. Clim.* **16**: 1456–1475.

Ogura Y, Takahashi T. 1971. Numerical simulation of the life cycle of a thunderstorm cell. *Mon. Weather Rev.* **99**: 895–911.

Petterssen S. 1956. *Weather Analysis and Forecasting*, Vol. 1. McGraw Hill: New York, NY.

Pokhrel S, Sikka D. 2013. Variability of the *TRMM*-PR total and convective and stratiform rain fractions over the Indian region during the summer monsoon. *Clim. Dyn.* **41**: 21–44.

Rajeevan M, Bhate J, Kale J, Lal B. 2005. Development of a high resolution daily gridded rainfall data for the Indian region. *Meteorol. Monogr.* **22**: 2005.

Rajeevan M, Bhate J, Kale J, Lal B. 2006. High resolution daily gridded rainfall data for the Indian region: Analysis of break and active monsoon spells. *Curr. Sci.* **91**: 296–306.

Ramanathan KR, Ramakrishnan KP. 1933. The Indian southwest monsoon and the structure of depressions associated with it. *Mem. India Meteorol. Dept.* **26**: 13–36.

Roca R, Bergès JC, Brogniez H, Capderou M, Chambon P, Chomette O, Cloché S, Fiolleau T, Jobard I, Lémond J, Ly M, Picon L, Raberanto P, Szantai A, Viollier M. 2010. On the water and energy cycles in the Tropics. *C. R. Geosci.* **342**: 390–402.

Roy SC, Roy AK. 1930. Structure and movement of cyclones in the Indian seas. *Beitr. Phys. Atmos.* **26**: 224–234.

Saha K, Sanders F, Shukla J. 1981. Westward propagating predecessors of monsoon depressions. *Mon. Weather Rev.* **109**: 330–343.

ⓒ 2016 The Authors. *Quarterly Journal of the Royal Meteorological Society* published by John Wiley & Sons Ltd on behalf of the Royal Meteorological Society.

Q. J. R. Meteorol. Soc. (2016)

Sarker RP, Choudhary A. 1988. A diagnostic study of monsoon depressions. *Mausam* **39**: 9–18.

Sassen K, Wang Z. 2008. Classifying clouds around the globe with the *CloudSat* radar: 1 year of results. *Geophys. Res. Lett.* **35**: L04805, doi: 10.1029/2007GL032591.

Short DA, Nakamura K. 2000. *TRMM* radar observations of shallow precipitation over the tropical oceans. *J. Clim.* **13**: 4107–4124, doi: 10.1175/1520-0442(2000)013<4107:TROOSP>2.0.CO;2.

Shukla J. 1978. CISK-barotropic-baroclinic instability and the growth of monsoon depressions. *J. Atmos. Sci.* **35**: 495–508, doi: 10.1175/1520-0469(1978)035<0495:CBBIAT>2.0.CO;2.

Sikka DR. 1977. Some aspects of the life history, structure and movement of monsoon depressions. *Pure Appl. Geophys.* **115**: 1501–1529.

Simpson J, Adler RF, North GR. 1988. A proposed tropical rainfall measuring mission (*TRMM*) satellite. *Bull. Am. Meteorol. Soc.* **69**: 278–295.

Simpson J, Kummerow C, Tao WK, Adler RF. 1996. On the tropical rainfall measuring mission (*TRMM*). *Meteorol. Atmos. Phys.* **60**: 19–36.

Sindhu K, Bhat G. 2013. Comparison of *Cloudsat* and *TRMM* radar reflectivities. *J. Earth Syst. Sci.* **122**: 947–956.

Sørland SL, Sorteberg A. 2015. The dynamic and thermodynamic structure of monsoon low-pressure systems during extreme rainfall events. *Tellus* **67**: 27039, doi: 10.3402/tellusa.v67.27039.

Stano G, Krishnamurti TN, Vijaya Kumar TSV, Chakraborty A. 2002. Hydrometeor structure of a composite monsoon depression using the *TRMM* radar. *Tellus A* **54**: 370–381, doi: 10.1034/j.2002.01330.x.

Stein TH, Parker D, Delanoë J, Dixon N, Hogan RJ, Knippertz P, Maidment R, Marsham J. 2011. The vertical cloud structure of the West African monsoon: A 4 year climatology using *CloudSat* and CALIPSO. *J. Geophys. Res. Atmos.* **116**: D22205, doi: 10.1029/2011JD016029.

Steiner M, Houze RA, Yuter SE. 1995. Climatological characterization of three-dimensional storm structure from operational radar and rain-gauge data. *J. Appl. Meteorol.* **34**: 1978–2007.

Stephens GL, Vane DG, Boain RJ, Mace GG, Sassen K, Wang Z, Illingworth AJ, O'Connor EJ, Rossow WB, Durden SL, Miller SD, Austin RT, Benedetti A, Mitrescu C. 2002. The *CloudSat* mission and the *A-Train*: A new dimension of space-based observations of clouds and precipitation. *Bull. Am. Meteorol. Soc.* **83**: 1771–1790.

Stephens GL, Vane DG, Tanelli S, Im E, Durden S, Rokey M, Reinke D, Partain P, Mace GG, Austin R, L'Ecuyer T, Haynes J, Lebsock M, Suzuki K, Waliser D, Dong W, Kay J, Gettelman A, Wang Z, Marchand R. 2008. *CloudSat* mission: Performance and early science after the first year of operation. *J. Geophys. Res. Atmos.* **113**: D00A18, doi: 10.1029/2008JD009982.

Tripoli G. 1992. An explicit three-dimensional nonhydrostatic numerical simulation of a tropical cyclone. *Meteorol. Atmos. Phys.* **49**: 229–254.

Wang Z, Sassen K. 2007. 'Level 2 cloud scenario classification product process description and interface control document'. http://www.cloudsat.cira.colostate.edu/sites/default/files/products/files/2B-CLDCLASS_PDICD.P_R04.20070724.pdf (accessed 23 November 2015).

Yoon JH, Chen TC. Water vapor budget of the Indian monsoon depression. *Tellus A* **57**: 770–782, doi: 10.1111/j.1600-0870.2005.00145.x.

Young MP. 2015. 'Improved rainfall monitoring for Africa', PhD thesis. University of Reading: UK.

Yuter SE, Houze RA. 1995. Three-dimensional kinematic and microphysical evolution of Florida cumulonimbus. Part II: Frequency distributions of vertical velocity, reflectivity, and differential reflectivity. *Mon. Weather Rev.* **123**: 1941–1963.

Zhao S, Mills GA. 1991. A study of a monsoon depression bringing record rainfall over Australia. Part II: Synoptic-diagnostic description. *Mon. Weather Rev.* **119**: 2074–2094.